



OPEN ACCESS

EDITED BY

Isaac Vidana,
Ministry of Education, Universities and
Research, Italy

REVIEWED BY

Carlos Frajuca,
Federal University of Rio Grande, Brazil
Ivano Lombardo,
Università di Catania, Italy

*CORRESPONDENCE

Angelo Pidotella,
pidotella@lns.infn.it

SPECIALTY SECTION

This article was submitted to Nuclear
Physics,
a section of the journal
Frontiers in Astronomy and Space
Sciences

RECEIVED 29 April 2022

ACCEPTED 03 August 2022

PUBLISHED 04 October 2022

CITATION

Pidotella A, Mascali D, Bezmalinovich M,
Emma G, Mazzaglia M, Mishra B,
Finocchiaro G, Galatà A, Marletta S,
Mauro GS, Naselli E, Santonocito D,
Torrise G, Cristallo S, La Cognata M,
Perego A, Spartà R, Tumino A and
Vescovi D (2022), Experimental and
numerical investigation of magneto-
plasma optical properties toward
measurements of opacity relevant for
compact binary objects.
Front. Astron. Space Sci. 9:931744.
doi: 10.3389/fspas.2022.931744

COPYRIGHT

© 2022 Pidotella, Mascali,
Bezmalinovich, Emma, Mazzaglia,
Mishra, Finocchiaro, Galatà, Marletta,
Mauro, Naselli, Santonocito, Torrisi,
Cristallo, La Cognata, Perego, Spartà,
Tumino and Vescovi. This is an open-
access article distributed under the
terms of the [Creative Commons
Attribution License \(CC BY\)](https://creativecommons.org/licenses/by/4.0/). The use,
distribution or reproduction in other
forums is permitted, provided the
original author(s) and the copyright
owner(s) are credited and that the
original publication in this journal is
cited, in accordance with accepted
academic practice. No use, distribution
or reproduction is permitted which does
not comply with these terms.

Experimental and numerical investigation of magneto-plasma optical properties toward measurements of opacity relevant for compact binary objects

Angelo Pidotella^{1*}, David Mascali¹, Matteo Bezmalinovich^{2,3},
Giulia Emma^{1,4}, Maria Mazzaglia¹, Bharat Mishra^{1,4},
Giorgio Finocchiaro^{1,4}, Alessio Galatà⁵, Salvo Marletta¹,
Giorgio Sebastiano Mauro¹, Eugenia Naselli¹,
Domenico Santonocito¹, Giuseppe Torrisi¹, Sergio Cristallo^{3,6},
Marco La Cognata¹, Albino Perego^{7,8}, Roberta Spartà¹,
Aurora Tumino^{1,9} and Diego Vescovi¹⁰

¹INFN, LNS, Catania, Italy, ²Department of Science and Technology, University of Camerino, Camerino, Italy, ³INFN, Sezione di Perugia, Perugia, Italy, ⁴Department of Physics and Astronomy, University of Catania, Catania, Italy, ⁵INFN, LNL, Legnaro, Italy, ⁶INAF, Osservatorio Astronomico d'Abruzzo, Teramo, Italy, ⁷Department of Physics, University of Trento, Trento, Italy, ⁸TIFPA, INFN, Trento, Italy, ⁹Department of Engineering and Architecture, University of Enna "Kore", Enna, Italy, ¹⁰Institute for Applied Physics, Goethe University Frankfurt, Frankfurt am Main, Germany

Electromagnetic transients known as kilonovae (KN), are among the photonic messengers released in the post-merger phase of compact binary objects, for example, binary neutron stars, and they have been recently observed as the electromagnetic counterpart of related gravitational-wave (GW) events. Detection of the KN signal plays a fundamental role in the multi-messenger astronomy entering in a sophisticated GW-detecting network. The KN light curve also delivers precious information on the composition and dynamics of the neutron-rich post-merger plasma ejecta (relying on *r*-process nucleosynthesis yields). In this sense, studying KN becomes of great relevance for nuclear astrophysics. Because of the highly heterogeneous composition, plasma opacity has a great impact both on radiative transport and spectroscopic observation of KN. Theoretical models attempting in encoding the opacity of this system often fail, due to the complexity of blending plethora of both light- and heavy-*r* nuclei transition lines, requesting for more complete atomic database. Trapped magneto-plasmas conceived in PANDORA could answer to these requests, allowing experimental in-laboratory measurements of optical properties and opacities, at plasma electron densities and temperatures resembling early-stage plasma ejecta's conditions, contributing to shed light on *r*-process metallic species abundance at the blue-KN diffusion time. A numerical study has been recently performed, supporting the choice of first physics cases to be investigated and the design of

the experimental setup. In this article, we report on the feasibility of metallic plasmas on the basis of the results from the systematic numerical survey on optical spectra computed under non-local thermodynamic equilibrium (NLTE) for several light- r nuclei. Results show the great impact of the NLTE regime of laboratory magneto-plasmas on the gray opacity contribution contrasted with those under the astrophysical LTE assumption. A first experimental attempt of reproducing ejecta plasma conditions has been performed on the operative Flexible Plasma Trap (FPT) at the INFN-LNS and here presented, together with first plasma characterization of density and temperature, *via* non-invasive optical emission spectroscopy (OES). The measured plasma parameters have supported numerical simulations to explore optical properties of NLTE gaseous and metallic plasmas, in view of the near-future plasma opacity measurements through spectroscopic techniques. The novel work so far performed on these under-dense and low-temperature magneto-plasmas, opens the route for the first-time to future in-laboratory plasma opacity measurements of metallic plasma species relevant for KN light curve studies.

KEYWORDS

plasma physics, nuclear astrophysics, multi-messenger astronomy, plasma spectroscopy, kilonovae

1 Introduction

The interplaying network of observations, combining both gravitational-wave (GW) signals and their electromagnetic (EM) counterparts, is representative of the outstanding window on the cosmos offered by multi-messenger astronomy (Rosswog, 2015). In this context, the mergers of compact binary (CB) objects—such as the coalescence of two neutron stars—provide a unique physical opportunity to advance knowledge on the heavy elements nucleosynthesis (Korobkin et al., 2012; Kasen et al., 2017), and to study the post-merger ejecta dynamics (Perego et al., 2014; Wu et al., 2022). The CB merger powers EM transient signals, following the GW event, known as *kilonovae* (Metzger, 2019) (hereafter, KN), which are fed by a peculiar balance of thermalization and radioactive heating processes (Li and Paczyński, 1998). Depending on the non-trivial merging dynamics and on the ejecta neutron richness, large neutron fluxes could lead to the production of n-rich isotopes far from the beta-stability valley, enriching the CB merger ejecta both of heavy (mass number $A \geq 140$) and light ($A \leq 140$) nuclei, synthesized *via* the rapid neutron capture nucleosynthesis process (r -process). The bolometric light curve broadband evolution of the bright optical transient AT2017gfo (Korobkin et al., 2012; Arcavi et al., 2017), detected after the GW170817 event (Abbott et al., 2017), has shown a fair agreement with the expected heating rate and opacity from freshly synthesized heavy elements (Metzger et al., 2010; Kasen et al., 2017), resulting from multi-component mass ejection and evolution. The r -process-powered KN transient emission has therefore a key role in the study of the complexity of r -process final abundance pattern, which relies on both thermodynamic conditions and radioactive decays. However, because of its heterogeneous composition, the CB merger ejecta *opacity* (κ) largely affects the KN emission, in turn influencing both the KN light-curve and the

spectral energy distribution. Opacity reflects the plasma atomic level population distribution and the related radiative cross sections. It regulates the energy exchange between plasma and radiation through several absorption-scattering reactions driven by a plethora of atomic line transitions (Tanaka et al., 2020). Ejecta enriched in light r -process elements result in low opacity ($\kappa \leq 1 \text{ cm}^2 \text{ g}^{-1}$), propagating optical light fading in days (*blue-KN*), whereas heavy r -process elements enlarges the opacity ($\kappa \gtrsim 10 \text{ cm}^2 \text{ g}^{-1}$), with redder light curves lasting even for weeks (*red-KN*) (Kasen et al., 2017). The color characterizing a specific phase of a KN event therefore acts as a diagnostics for the produced nuclei. However, state-of-the-art literature widely request for progresses on opacity modeling (Barnes and Kasen, 2013; Rosswog, 2015; Barnes et al., 2016; Metzger, 2019; Tanaka et al., 2020) to improve KN predictions. Indeed, limited experimental data on opacity of complex (d - and f -shell elements (Bailey et al., 2009; Hoarty et al., 2010; Zhang et al., 2011; Bailey et al., 2015), as well as of their level structure and reaction rates, along with atomic constraints provided by oversimplified theoretical models, could lead to inconsistent results if compared with observations. Therefore, an experimental benchmark closing the gap between theory and observations would be highly desirable to draw quantitative conclusions on the nucleosynthetic yield from observations. At the INFN-LNS, a new plasma trap called PANDORA is under construction (Mascali et al., 2022a). The trap has been developed within the INFN funded PANDORA (Plasma for Astrophysics, Nuclear Decays Observation and Radiation for Archaeometry) project, with the aim to study weak-interaction rates in controlled and monitored electron cyclotron resonance (ECR) plasmas, reproducing stellar-like conditions, in terms of temperature and ion charge state distribution, and opening the route to interdisciplinary experiments relevant for the astrophysics

and nuclear astrophysics. In the framework of opacity measurements interesting for the KN light-curve study, trapped magneto-plasmas conceived in PANDORA offer an outstanding controlled environment, allowing first-of-its-kind in-laboratory measurements of optical properties and opacities, at plasma electron densities and temperatures resembling early-stage plasma ejecta's conditions, contributing to shed light on *r*-process metallic species abundance at the blue-KN diffusion time. A numerical study has been recently performed, supporting the choice of first physics cases to be investigated and the design of the experimental setup (Pidatella et al., 2021). In this article, we report on further considerations about the possibility of producing metallic light *r*-process plasmas eligible for the opacity measurements, using the PANDORA plasma trap (Section 2.1). On this track, we report on the first experimental attempt of reproducing ejecta plasma conditions carried out on the already operative Flexible Plasma Trap (FPT) at the INFN-LNS (Section 2.2.1), presenting first plasma characterization of density and temperature (Section 2.2.2), via non-invasive optical emission spectroscopy (OES). The measured plasma parameters have supported numerical simulations to explore optical properties of non-local thermodynamic equilibrium (NLTE) gaseous and metallic plasmas (Section 2.3), in view of the near-future plasma opacity measurements using spectroscopic techniques. Results of in-plasma spectroscopic measurements and of numerical investigations on plasma optical properties is presented and discussed in (Sections 3.1, 3.2), respectively. Finally, conclusion and possible outlook of the work is provided in (Section 4).

2 Methods

In the following, we report on the methodologies and experimental techniques employed in this work. Technological aspects are discussed in Section 2.1, based on the know-how gained at the INFN laboratories (LNS and LNL) on injection methods of metallic atoms into magnetically confined plasmas, and on the numerical feasibility study (Pidatella et al., 2021), providing further constraints on the physics cases suitable for opacity measurements. Moreover, a full description of the flexible plasma trap facility, the experiment design, and diagnostics techniques employed are provided in Section 2.2. Finally, details on the numerical calculations performed to study magneto-plasma optical properties are reported in Section 2.3.

2.1 On kilonovae ejecta constraints for in-laboratory electron cyclotron resonance plasma experiments: Metallic element injection

Fundamental elements for the interpretation of the KN light-curve are the *r*-process yields (determining the heating term) and

opacities (leading the energy exchange between radiation and plasma). The AT2017gfo spectrum delivers absorption signatures suitable with blending of many atomic lines expected from actinides and lanthanides. For earlier-stages spectrum (~ 1.5 days), a prominent absorption feature compatible with *strontium* lines has been observed (Watson et al., 2019; Gillanders et al., 2022). Recently, the contribution to spectral features arising from *hydrogen* and *helium* was excluded (Perego et al., 2022), and other synthetic spectra calculations have reported about possible detection in future KN events of light elements such as *calcium* (Domoto et al., 2021), *platinum*, and *gold* (Gillanders et al., 2021). Despite the huge number of studies on KN light-curve predictions, still large uncertainties on the relative contributions from various isotopes remain, in part due to the lack of complete atomic transition data. In this view, we have recently performed a numerical study to draw feasibility conditions in the plasma trap for measuring opacity of some of these light elements, on the basis of inputs from KN ejecta models and *r*-process nucleosynthesis yields calculations (Pidatella et al., 2021). Inside a compact magnetic trap, such as PANDORA, dense and hot magneto-plasmas, composed of multi-charged ions in a bath of energetic electrons, are magnetically confined, and heated by microwave power, exploiting the ECR heating mechanism (Geller, 1996). ECR plasma typical electron densities go up to $\sim 10^{13} \text{ cm}^{-3}$ and energies in the range of eV- tens of keV (Mascali et al., 2022a). Within these plasma conditions, the KN stage reproducible in the trap belongs to $10^{-2} - 10^0$ days after the merger, corresponding to the *blue-KN* signal. The latter shows a peak of the light curve at optical frequencies, mostly determined by ejecta's light component with low opacity. The light *r*-process elements production is expected to be prominent at this stage, due to high *electron fraction* Y_e , this being indicative of the initial neutron richness. Since the blue-KN is largely shaped by light elements, the study was focused on plasma atomic species going from *selenium* ($Z = 34$) to *rhodium* ($Z = 45$). While theoretical predictions, based only on abundances and number of transition lines, promote elements as molybdenum, technetium, ruthenium, and rhodium as the most opaque species among those considered (Tanaka et al., 2020), we found that at typical NLTE regime and plasma parameters studied, the mean opacities of lighter elements as selenium, strontium, zirconium, and niobium are several orders of magnitude larger than those of the former elements (Pidatella et al., 2021). Injection of the aforementioned *metallic* elements in ECR plasmas requires specific vaporization techniques, both using *resistive ovens* (RO) to evaporate the metallic compound whose vapor pressure goes to 10^{-2} mbar at temperature $T \leq 2000$ K, or *sputtering* (Sp) techniques, usually used for refractory elements. The choice of methods also depends on the efficiency of injection (Mascali et al., 2022a; Mauro et al., 2022). On this basis, selenium and strontium are chosen as day-0 cases for the first measurements. In Table 1, we report on the results from injection efficiency calculations carried out on the aforementioned elements. It can be evinced that some elements

TABLE 1 Light *r*-process elements of interest for opacity measurements for the blue-KN stage. T_{vap} [K] is the evaporation temperature of the species. Species with larger injection efficiency and easier production are marked in green (■), while those presenting some efficiency or availability limitations in yellow (■).

	T_{vap} [K]	Compound	Method	Note
Se	500 (oven)	Se	RO/Sp	Low T_{vap} could be difficult to control.
Sr	796	Sr	RO	Handling rules typical of alkaline earth metals.
Zr	–	Zr	Sp	Yield: 1 atom/ion at 67.1 eV.
Nb	–	Nb	Sp	Yield: 0.9 atom/ion at 65.6 eV.
Mo	1073	MoO ₃	RO	Used at LNL to produce Mo beams. Temperature stability requested.
Tc	–	Tc	Sp	Yield: 5.5 atom/ion at 17.1 eV. Radioisotope suppliers.
Ru	–	Ru	Sp	Yield: 1.8 atom/ion at 41.5 eV.
Rh	–	Rh	Sp	Yield: 2.1 atom/ion at 36.4 eV.

are more feasible than other, both in terms of availability, handling/control of the injection procedure, and efficiency.

2.2 First characterization of plasma parameters for gaseous electron cyclotron resonance plasmas

In this section, the main characteristics of the FPT are highlighted. The trap represents the outcome of the experience gained in the physics of plasma ion source at the INFN-LNS in the last decades (Gammino et al., 2017). It is characterized by a peculiar flexibility in terms of possible magnetic field configurations and microwaves heating frequency, exploiting the known ECR heating mechanism (Geller, 1996). Plasma parameters mostly depend on the particular tuning of the field profile, RF frequency and power, and gas buffer pressure, leading to many possible scenarios. Generated plasmas are suitable for studies of astrophysics, nuclear, and multidisciplinary physics, especially on the basis of their stellar-like temperature conditions. In this context, a particular effort has been spent at the INFN-LNS to develop a multi-diagnostics system to allow both a full characterization of the plasma parameters for all electron and ion species involved and interdisciplinary studies (Mazzaglia et al., 2018; Naselli et al., 2019a; Mazzaglia et al., 2019; Naselli et al., 2022a; Mascali et al., 2022b; Torrisi et al., 2022). The FPT is therefore a valuable experimental facility operative at the INFN-LNS to benchmark monitoring diagnostics and experimental techniques to be employed in PANDORA, of course on a larger scale, which is precious for the future envisaged in-laboratory plasma measurements relevant for the KN study. In the following, we report on the experimental setup adopted for the first non-invasive characterization of gaseous ECR plasma only via OES, generated, confined, and sustained via the FPT (Section 2.2.1). We also provide a general picture of the multi-diagnostic

setup used in the experiment, particularly focusing on OES diagnostic, and the applied line-ratio method (Fantz, 2006; Fantz et al., 2006) for estimating electron plasma density and temperature for low-Z plasma buffer (Section 2.2.2), that is, hydrogen (H₂) and argon (Ar).

2.2.1 Experimental setup: Flexible plasma trap and diagnostic system

The FPT magnetic field is provided by means of three solenoids, which allow the tuning of the field profile. The plasma characterization in the FPT has been performed in both *simple mirror* and *quasi B-flat* configuration, adequately tuning the $B_{\text{min}}/B_{\text{ECR}}$, used as figure of merit for the plasma stability (Mazzaglia et al., 2018; Naselli et al., 2019b), and also modifying source parameters: microwave power (P_{RF}), heating frequency (f_{RF}), and gas neutral pressure (p_0). In the Figure 1A view of the FPT setup including all diagnostics used is shown. The FPT plasma has been generated via the radial microwave injection (perpendicular to the chamber longitudinal axis), leaving the parallel axis available for the diagnostics. The injection is carried at frequencies ranging between 4 and 7 GHz. The signal is generated by a Rohde & Schwarz generator, amplified by a traveling wave tube (TWT) and sent to the FPT by WRD350 waveguides. A directional coupler allows to measure forward and reflected power, while an insulator safeguards the TWT by the power reflected backward. A differentially pumped system, using a small orifice (dosing valve), connects the plasma chamber vacuum with the vacuum reservoir developed for performing mass spectrometry. The two vacuum systems work at very different pressures (e.g., $p_{\text{chamber}} = 10^{-4+2}$ mbar, $p_{\text{spectrometer}} \leq 10^{-5}$ mbar) and requires the development of an independent vacuum piping system. A compact residual gas analyzer (RGA) was used for the vacuum diagnostics and for mass spectroscopy (Pfeiffer Vacuum—QMG 250 PrismaPro®). A view of the apparatus is shown in Figures 1C,D. The diagnostic line is quite complex, with

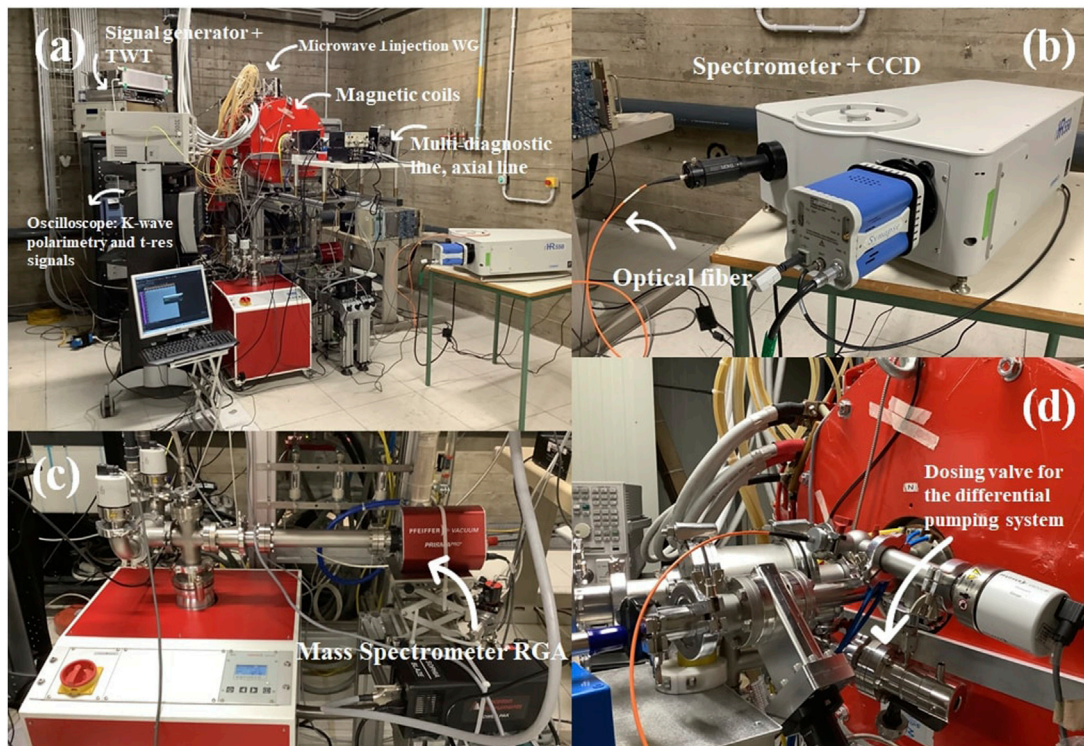


FIGURE 1

FPT experimental room and apparatus. (A) View of the FPT setup, including the chamber, magnetic coils, the RF instrumentation, and the axial diagnostic line. (B) Horiba spectrometer and the CCD detector, connected to the optical fiber. (C) RGA and the differential pumping system set to perform mass spectroscopy of gases in the chamber. (D) Part of the X-ray diagnostic line, with focus on the orifice to dose gas into the RGA.

the intent to perform non-invasive on-line cross-measurements in multi-diagnostics:

- 1) A pin-hole setup, coupled to a high-resolution CCD camera, able to perform space-resolved X-ray imaging of plasma emission (Rácz et al., 2016). The system is supported by an algorithm, which can analyze the single-photon counting (SPHC) images for energy-resolved investigation pixel-by-pixel to study the local plasma-emitted spectrum in a high-dynamic range (HDR) mode by distinguishing the fluorescence lines of the materials of the plasma chamber (Ti and Ta) from plasma, for example, (Ar) fluorescence lines (Naselli et al., 2022b);
- 2) OES has been developed to characterize the cold electron population ($k_B T_e \leq 30$ eV). It consists of an energy-calibrated spectrometer (*i*-HR 550 Horiba, diffraction grating 2,400 gr/mm, with nominal resolution of 35 pm at 486 nm, ranging from 300 to 750 nm), with relative calibration in intensity, coupled to a CCD detector (26 μm pixels)—a view of the detection system is shown in Figure 1B. OES allows not only to estimate the electron density and temperature of cold electrons in the plasma bulk (Mazzaglia et al., 2019) but also to advance knowledge on the relative percentage of the ion species

within the plasma, by means of the *line-ratio method* (Fantz, 2006);

- 3) Microwave interfero-polarimetry to measure the line-of-sight integrated density of the whole plasma. Microwave polarimetry setup is able to investigate on the magnetoplasma-induced Faraday rotation in a compact plasma trap, monitoring plasma ignition, stability, and whole-density modulation led by changes in the source parameters (Mascali et al., 2022b);
- 4) RF probe placed axially and connected to an 80 Gsample/s oscilloscope, included to probe kinetic plasma instability and to make time-resolved measurements of the latter, based on the detection of emitted RF signals from the unstable plasma.

In this work, despite the synergistic effort spent to develop the aforementioned diagnostic system, we will only provide further insights on the OES diagnostic (b), and its related methods to investigate on optical properties of generated plasmas.

2.2.2 Plasma optical emission spectroscopy for hydrogen and argon plasmas

To interpret intensities measured by OES, a model describing the correlation between atomic level population densities of excited states with plasma parameters, for example, the

electron density (ρ_e) and, if the electron energy distribution function (EEDF) is Maxwellian, the electron temperature (T_e) must be used. Collisional-radiative (CR) models well suite typical NLTE plasma generated *via* the ECR mechanism (Fantz, 2006; Fantz et al., 2006). The models provide this description by balancing reactions that imply a change in the electron energy level of atoms or molecules in a plasma: the time-derivative of the population density n_p of an excited state p can be written as a function of the other state densities,

$$\frac{dn_p}{dt} = \sum_{q>p} n_q A_{qp} - \sum_{q<p} n_p A_{pq} + \rho_e \left(\sum_{q \neq p} n_q \chi_{q \rightarrow p} - \sum_{q \neq p} n_p \chi_{p \rightarrow q} \right), \quad (1)$$

with ρ_e being the electron density, A_{qp} is the Einstein coefficient for the transition from state q to p , $\chi_{q \rightarrow p}$ is the rate coefficient for electron collision excitation (if $E_q \leq E_p$) and de-excitation (if $E_q \geq E_p$). This quantity describes, given an initial and a final state, the number of considered electron collision processes per unit of time normalized by the densities of the colliding particles. In Eq. 1, by taking $p = 1, \dots, N$, with N being the total number of excited levels of the considered emitting particle specie, a whole set of coupled differential equations, describing the temporal evolution of the population density of each excited state, is obtained. Such set is a simplified example of a CR model, which includes some of the most relevant processes for a low-pressure and low-temperature plasma. However, more processes can be included making models progressively closer to the reality. The resulting population densities n_p can be written in terms of population coefficients, $R_{0p} = n_p / (n_0 \cdot \rho_e(T_e))$, with n_0 being the ground state density, and n_p a function of ρ_e , as seen from Eq. 1. Since population coefficients are function of plasma parameters, they can be used to reproduce/match experimental measurements, and in particular to determine *averaged* electron density and temperature, inferred *via* emission-line ratios from plasma spectroscopy, along the line-of-sight. In this work, the Yacora CR model (Wunderlich et al., 2020) has been used, in which calculations assume only excitation from the respective ground state in both the atom and the molecule, mainly for diagnostics in low-pressure plasmas (namely for atomic hydrogen, molecular hydrogen, and helium). Line ratio, between two different emission wavelengths λ_j and λ_k , R_{λ_j/λ_k} , can be obtained by evaluating the ratio between effective emission rate coefficients,

$$R_{\lambda_j/\lambda_k} = \frac{\chi_{eff}^{em}(\lambda_j; \rho_e, T_e)}{\chi_{eff}^{em}(\lambda_k; \rho_e, T_e)} \propto \frac{I(\lambda_j)}{I(\lambda_k)}. \quad (2)$$

Thus, the line-ratio method only requires the analyzed spectra to have relatively calibrated their lines, making it more viable since no absolute intensity calibration is needed. However, the method is not fully exploitable for absolute information carried by single-line emission, leaving a possible full line interpretation only to absolutely calibrated spectra. With this limitation in mind, in the following we will present results on the basis of the line-ratio

method, supported by a complete error analysis above the experimental results and the estimated plasma parameters. Several configurations of the plasma trap have been explored, and systematic data acquisition has been carried out. All spectra have been measured collecting the visible (VIS) light in the range 350–750 nm, *via* an optical fiber (NA = 0.22, core $\phi = 200 \mu\text{m}$), connecting the spectrometer to a quartz window of a vacuum flange (see Figure 1D). Different acquisitions, ranging in 1–2 s, have been used dependent on the RF power employed to sustain the plasma. Figure 2 shows both magnetic field profiles used to confine the plasma and typical spectra collected in the VIS for both single-H₂ and H₂-Ar gas-mixture plasma. Further information on each experimental run are reported in Table 2.

2.3 Numerical investigation on electron cyclotron resonance plasma optical properties

Experimental activities would widely benefit of numerical studies of the plasma optical properties. The latter shows not only interesting properties as being an *active* medium but also ECR magneto-plasmas in trap are present with peculiar properties, such as high inhomogeneity and anisotropic energy distribution, due to the EM heating and the magnetic confinement. Therefore, in-laboratory ECR plasmas become an interesting physical *mean* to be described in terms of radiation–matter coupling, in order to support the envisaged experimental spectroscopic measurements. In the following, we present some numerical results concerning the impact of a *layered* plasma mean on the optical features of the plasma, in terms of varying electron density and temperature along one line-of-sight, including or not the presence of an external perturbing black-body radiation field (Section 2.3.1). By means of the same numerical approach, we provide some quantitative constraints on typical light-source properties, which can be compatible with the maximization of plasma opacity at given electron density and temperature, resulting from the OES experimental measurements (Section 2.3.2).

2.3.1 Impact of non-homogeneous plasma stratification on transmission spectroscopy

The problem of determining plasma parameters and structure from optically thin emission lines, whose emission coefficients and frequency-integrated intensities depend on both electron temperature and density, is widely discussed in the literature (Craig and Brown, 1976; Thompson et al., 1992), especially facing the fundamental limitations of observed spectral line-ratios as well-posed diagnostic method for inferring plasma parameters (Judge and Hubeny, 1995; Judge et al., 1997). The *inverse problem* is affected by large uncertainties in the case of non-isothermal and inhomogeneous emitting source, since the latter could be structured and layered along the line-of-sight of the detector, thus producing a *convoluted* spectral distribution

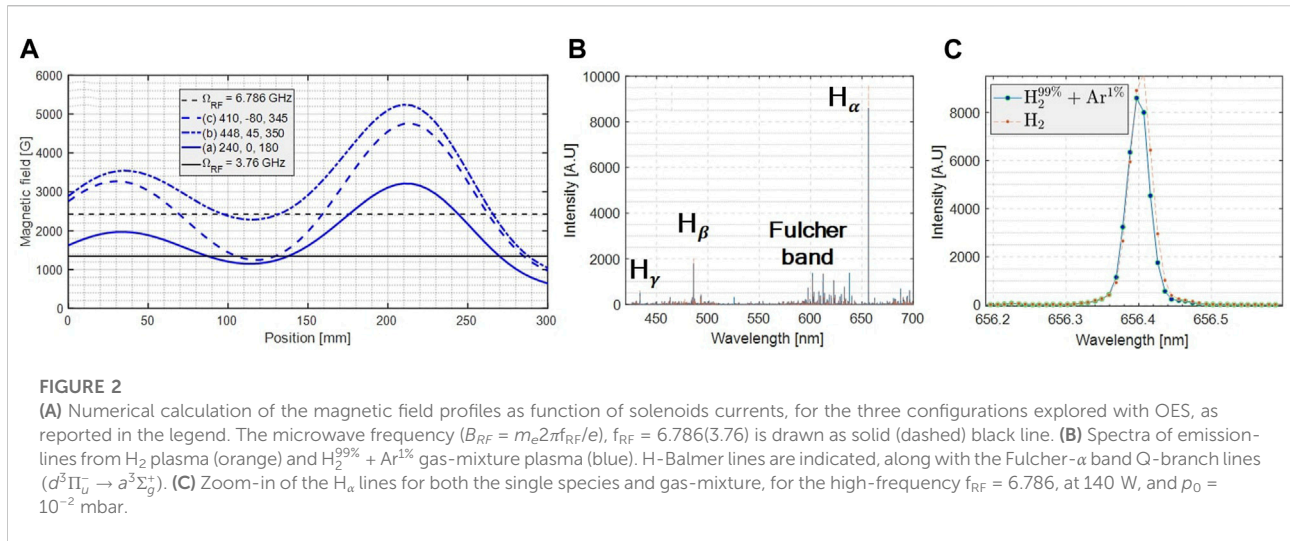


FIGURE 2

(A) Numerical calculation of the magnetic field profiles as function of solenoids currents, for the three configurations explored with OES, as reported in the legend. The microwave frequency ($B_{RF} = m_e 2\pi f_{RF} / e$), $f_{RF} = 6.786(3.76)$ is drawn as solid (dashed) black line. (B) Spectra of emission-lines from H_2 plasma (orange) and $H_2^{99\%} + Ar^{1\%}$ gas-mixture plasma (blue). H-Balmer lines are indicated, along with the Fulcher- α band Q-branch lines ($d^3\Pi_u^- \rightarrow a^3\Sigma_g^+$). (C) Zoom-in of the H_α lines for both the single species and gas-mixture, for the high-frequency $f_{RF} = 6.786$, at 140 W, and $\rho_0 = 10^{-2}$ mbar.

TABLE 2 OES experimental run details. Pure hydrogen (H_2) and hydrogen-argon mixture ($H_2^{99\%} + Ar^{1\%}$) cases are explicitly indicated. Configurations are labeled by n. (#) and B-field (a-c) - see also Figure 2A.

	B_{max}/B_{min}	f_{RF} [GHz]	p_0 [mbar]	P_{RF} [W]	t_{acq} [s]	N. of spectra
# 1, (a), H_2	2.7930	3.76	$9E - 04$	100 ÷ 250	1	10
# 2, (a), H_2	2.7930	3.76	$1E - 02$	100 ÷ 400	1	10
# 3, (a), $H_2^{99\%} + Ar^{1\%}$	2.7930	3.76	$1E - 02$	100 ÷ 350	1	10
# 4, (b), H_2	2.2945	6.774	$1E - 03$	40 ÷ 120	1	10
# 5, (c), H_2	3.8289	6.786	$1E - 03$	40 ÷ 100	2	5
# 6, (c), H_2	3.8289	6.786	$1E - 02$	40 ÷ 140	2	5
# 7, (c), $H_2^{99\%} + Ar^{1\%}$	3.8289	6.786	$1E - 02$	40 ÷ 140	2	5

with an emission measure differential both in density and temperature. These layered-emission properties can be easily related to ECR plasmas. Therefore, studying this spectroscopic problem is of relevant interest for supporting experimental measurements. In this context, we performed numerical calculations of synthetic spectroscopic observables of emitting ECR plasmas, with a layered structure along one line-of-sight, at specific electron density and temperature. These latter are taken from previous self-consistent numerical simulations (Mishra et al., 2021) carried out to reproduce experimentally observed X-ray fluorescence emission of argon plasma, magnetically confined in a *minimum-B* profile, ignited, and sustained with microwave frequency and power, 12.84 GHz and 30 W, respectively. The numerical tool used is able to collect plasma electrons with similar parameters (density, EEDF) in regions of interest (ROIs) based on their *mean energy* content. *Clustering* of electrons in ROIs has been performed looking at electrons in the [0,2] keV energy range, along the longitudinal axis of the plasma chamber, crossing, the closed resonating magnetic isosurface at $B = B_{ECR} = 0.46$ T, as well as one of the employable spectroscopic

line-of-sight designed for the plasma trap. Figure 3 shows the collection of nested mean energy isosurfaces inside the simulation domain, along with the ECR isosurface. A multi-slicing plot is superimposed on this, providing a cross-view of the space-dependent plasma's electron mean energy upon moving along the longitudinal axis. Seven main ROIs have been located here and are indicated as R in the figure. For each of these ROIs, one collective electron density and temperature (assuming a Maxwellian EEDF) is assigned. This simulation allows us to provide a hint of the structured plasma parameters along the experimental line. Electron density and temperature estimated supply the next numerical calculations by means of the ion population kinetics code known as FLYCHK (Chung et al., 2005). The code suite takes as inputs the plasma parameters to compute spectral observables of the plasma, such as opacity, emissivity, and intensity, according to the degree of plasma ionization and atomic level population distribution. Calculations have been performed in NLTE regime, which is typical of ECR sources, by solving the rate matrix equations arising from the CR model considered in the code suite, including

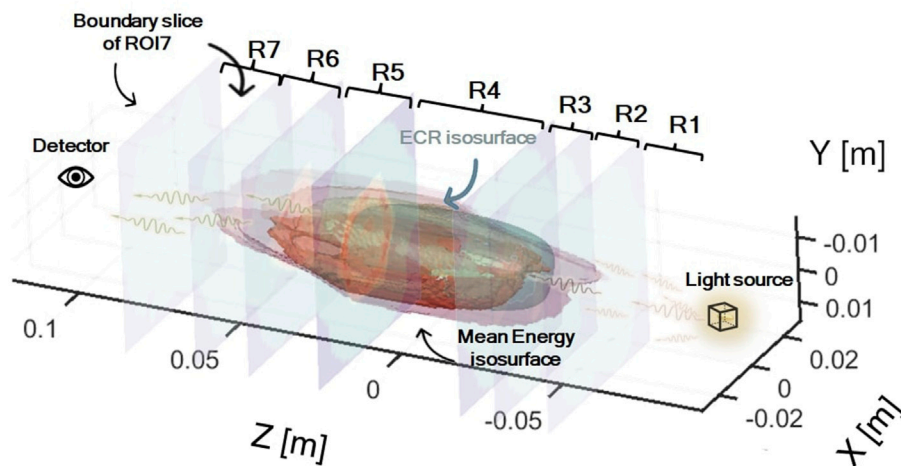


FIGURE 3 Representation of simulated plasma slicing along the longitudinal z-axis for studying the layered optical properties of Ar plasma. Nested isosurfaces refer to the volumetric collection of electron with the same mean energy content. Magnetic isosurface at the ECR (light-blue) is also shown. Along the z-axis regions of interest (R) have been selected and indicated in the figure, intersecting inhomogeneous plasma regions with different electron density ρ_e and energy $k_B T_e$, both numerically extracted in the [0,2] keV energy interval, and associated to each R. All the R is assumed as homogeneous plasma slab to be studied in FLYCHK, in the presence or not of a light source black-body radiation field.

both the collisional and radiative processes. The code is also capable to include the effects of external radiation field, on the basis of an input file containing the intensity of the source as a function of the radiation wavelength, which has been included and processed in our calculations. This latter has been performed to show the impact of a light source on the stratified optical properties of plasmas. Focusing on the numerical structure of opacity, this is computed in terms of the cross section for both *bound-bound* transitions (κ^{BB}), *bound-free* transitions (κ^{BF}), and *free-free* transitions (κ^{FF}). Radiation from BB transition peaks at a wavelength corresponding to the energy difference between two levels. BF transition is recombination radiation, whose wavelength corresponds to the sum of the kinetic energy of the recombining electron and the binding energy of the shell that the electron falls to. Bremsstrahlung radiation is emitted from FF transitions when free electrons lose their kinetic energy colliding with electrons or ions. While the FF process involves continuum states, whose opacity mostly depends on electron density and temperature, the BF and BB also depend on the ion stage population of excited levels in the atomic shell. For instance, the BB opacity is given as

$$\kappa_{\lambda}^{BB} = N_{\ell} \left(1 - \frac{N_u g_{\ell}}{N_{\ell} g_u} \right) \frac{\pi e^2}{\rho m c} f_{\ell u} \varphi_{\lambda} \quad [\text{cm}^2 \text{g}^{-1}], \quad (3)$$

where the population density of the upper (lower) level is $u(\ell)$, $N_u(N_{\ell})$, $g_u(g_{\ell})$ are the degeneracy factors, ρ [g cm^{-3}] is the density of the specie, $f_{\ell u}$ is the oscillator strength, and φ is the line profile function. At low-temperature blue-KN ejecta conditions ($T \leq 10^4$ K), together with a low ionization level, typically κ^{BB}

results to be prominent among the other terms. The numerical results from calculations of the plasma opacity including all three possible contributions, and performed for the argon plasma as structured from self-consistent simulations are presented and discussed in Section 3.2.

2.3.2 Light-source dimensioning for electron cyclotron resonance plasma spectroscopy based on optical emission spectroscopy measurements

Numerical calculations by using FLYCHK can also support the experimental design, and in particular the light-source dimensioning in terms of power and/or spectral irradiance to be used for transmission spectroscopy, and for measuring the line-integrated opacity of emitting plasma. We have performed calculations of synthetic spectral observables, focusing on the opacity term, to study the impact of external black-body radiation fields on the latter, for gaseous as well as for metallic species of interest for the KN studies. Contrarily to what has been carried out about the layered plasma emission, described earlier in Section 2.3.1, plasma parameters used in these calculations are not derived from 3D numerical simulations, but rather they are constrained by the estimates from OES observations during the experiment, as described in Section 2.2.2, which results are present in Section 3.1. In doing this, we have assumed plasma parameters for metallic plasmas similar to the gaseous experimentally explored so far, given that metallic species atom fractions with respect to the plasma buffer gas (e.g., Ar) is usually not exceeding 1 %. Moreover, and for

simplicity, no structured emission is considered in these calculations, but a rather homogeneous emitting plasma source. We aim at finding a good experimental trade-off among light-source intensity and the evidence of more opaque spectral region, whose absorption feature are better observable during the transmission measurements.

3 Results and discussion

In the following, we report on the experimental data collected *via* OES, and on the data analysis performed to estimate both electron density and temperature, along with their experimental uncertainties, as resulting from the line-ratio method applied to the hydrogen Balmer’s lines (H_{α} , H_{β} , and H_{γ}). Moreover, numerical results concerning the plasma optical properties arose by the calculations with FLYCHK will be presented, focusing on the predicting power of simulations to support future experimental measurements, as well as to investigate on the plasma stratification problem, and thus on the light-emission convolution, along experimental line-of-sights.

3.1 Experimental data analysis

Several plasma trap configurations (hereafter, *cfgs*) have been investigated, but only seven of these have been chosen to make systematics in terms of RF power (P_{RF}), based on the plasma stability and reproducibility, as reported in Table 2. The latter, beyond the capability of the plasma trap to engage, ignite, and sustain, the plasma at a given frequency (f_{RF}) and magnetic confinement, has been probed *via* OES by looking at the stability of $H_{\alpha,\beta,\gamma}$ emission lines, and in particular on their ratios, that is, $H_{\alpha\beta} = H_{\alpha}/H_{\beta}$, and $H_{\beta\gamma} = H_{\beta}/H_{\gamma}$, during many acquisitions at fixed P_{RF} . Example of such on-line analysis is shown in Figures 4A,B for one of the configurations. The ratios employed for monitoring are calculated from the analysis performed on each spectrum. A dedicated code written in MATLAB[®] has been developed to perform the spectral analysis, by means of least-square fit procedure of emission peak of interest, along with the error derivation from the fit procedure. Multiple-Gaussian fits are employed to improve the fit procedure, and the peak area is used as a central value of the ratios. In the end, the error analysis including both statistical error and uncertainty led by the fit procedure is computed *via* the error propagation formulas. The following analysis flow is considered:

- Fitting procedure on the peaks of the H-spectra. The general formula for the peak’s area calculation fit by N Gaussian function ($f(\lambda) = a \cdot \exp(-(\lambda - b)^2/c^2)$), is given as

$$A_{\lambda_j} = \sum_{i=1}^N \frac{a_i \cdot c_i \cdot \sqrt{\pi}}{\Delta\lambda}, \quad (4)$$

where N is the number of Gaussian functions used, a_i , c_i , are the i -th coefficients from fit parameters, $\Delta\lambda$ is the spectral bin width. Areas of the peaks refer to the related line-intensities, and to the population rate coefficients, accordingly to Eq. 2.

- Calculation of the ratios, $H_{\alpha\beta} = A_{\lambda_{\alpha}}/A_{\lambda_{\beta}}$ and $H_{\beta\gamma} = A_{\lambda_{\beta}}/A_{\lambda_{\gamma}}$ for each spectrum and for all the configurations.
- Error propagation procedure to estimate uncertainties. For each spectrum, each calculated area below the peaks carries an error, given as

$$\delta A_{\lambda_j} = \sqrt{\sum_{i=1}^N \left[\left(\frac{\partial A_{\lambda_j}}{\partial a_i} \right)^2 \sigma_{a_i}^2 + \left(\frac{\partial A_{\lambda_j}}{\partial c_i} \right)^2 \sigma_{c_i}^2 + 2\sigma_{a_i c_i} \frac{\partial A_{\lambda_j}}{\partial a_i} \frac{\partial A_{\lambda_j}}{\partial c_i} \right]}, \quad (5)$$

with $\sigma_{a,c}$ the standard deviation on a , c fit coefficients, and σ_{ac} the correlation coefficients from the covariance matrix. The latter terms contribute to the total error only in case of correlations among the fit coefficients in the Eq. 4. The covariance analysis has shown generally non-zero correlation elements σ_{ac} which however are negligible with respect the other terms, and hence they have been ruled out from later on estimates of errors. By means of Eqs 4, 5, error propagates also to the ratios as

$$\begin{aligned} \delta H_{\alpha\beta} &= H_{\alpha\beta} \sqrt{\left(\frac{\delta A_{\lambda_{\alpha}}}{A_{\lambda_{\alpha}}} \right)^2 + \left(\frac{\delta A_{\lambda_{\beta}}}{A_{\lambda_{\beta}}} \right)^2}, \\ \delta H_{\beta\gamma} &= H_{\beta\gamma} \sqrt{\left(\frac{\delta A_{\lambda_{\beta}}}{A_{\lambda_{\beta}}} \right)^2 + \left(\frac{\delta A_{\lambda_{\gamma}}}{A_{\lambda_{\gamma}}} \right)^2}. \end{aligned} \quad (6)$$

- Since we have a set of S independent measurements of the peaks area, each of them equally important, but with some of them carrying unequally large uncertainties, it is sounder computing the so-called *inverse variance weighting*, onto a *weighted mean* of ratios, which gives more weight to the measurements with less uncertainty (Taylor, 1996; Knoll, 2010). Thus, we proceed calculating the weighted mean ratio for each configuration, $\langle H_{\alpha\beta} \rangle$ and $\langle H_{\beta\gamma} \rangle$, according to

$$\langle H_{\alpha\beta,\beta\gamma} \rangle = \frac{\sum_{i=1}^S w_i^{\alpha\beta,\beta\gamma} H_{\alpha\beta,\beta\gamma}}{\sum_{i=1}^S w_i^{\alpha\beta,\beta\gamma}}, \quad (7)$$

with $w_i^{\alpha\beta,\beta\gamma} = 1/\delta H_{\alpha\beta,\beta\gamma}^2$ being the weights obtained through Eq. 6. The standard error associated to Eq. 7 can be then computed by applying the propagation formula to the latter (Knoll, 2010), which is given as

$$\begin{aligned} \sigma_{\langle H_{\alpha\beta,\beta\gamma} \rangle}^2 &= \frac{\sum_{i=1}^S w_i^{\alpha\beta,\beta\gamma} (H_{\alpha\beta,\beta\gamma} - \langle H_{\alpha\beta,\beta\gamma} \rangle)^2}{\sum_{i=1}^S w_i^{\alpha\beta,\beta\gamma}} \frac{n_{eff}}{n_{eff} - 1}, \\ \text{with } n_{eff} &= \frac{\left(\sum_{i=1}^S w_i^{\alpha\beta,\beta\gamma} \right)^2}{\sum_{i=1}^S (w_i^{\alpha\beta,\beta\gamma})^2}. \end{aligned} \quad (8)$$

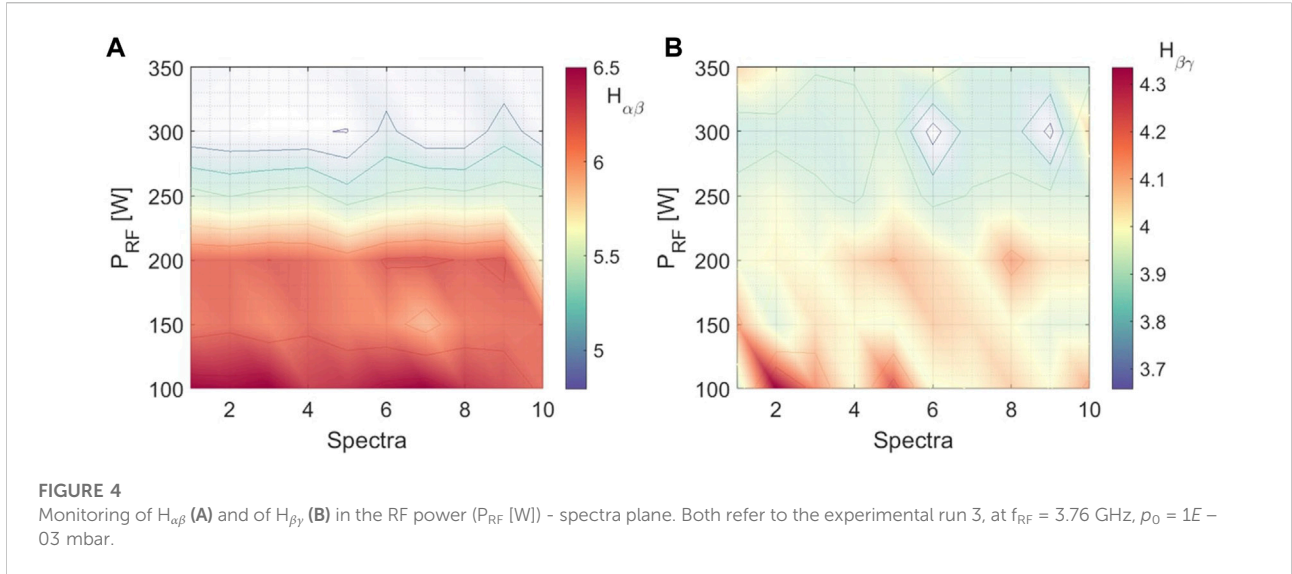


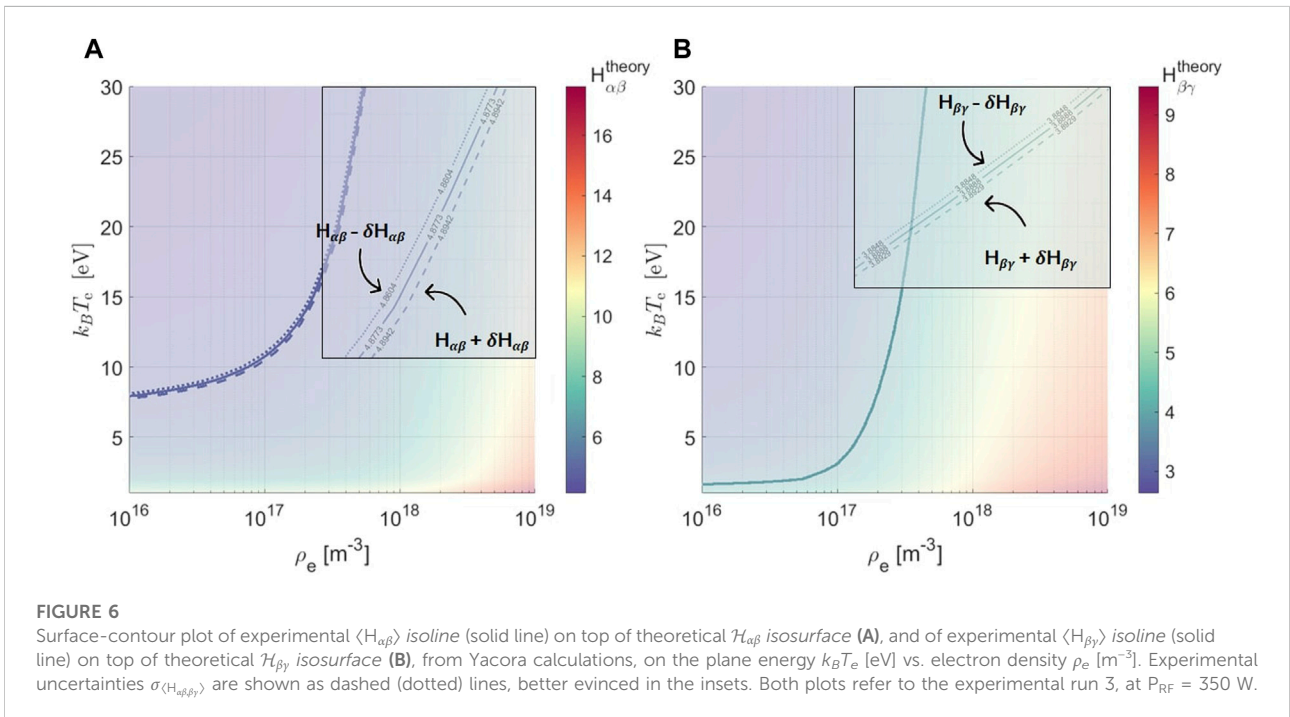
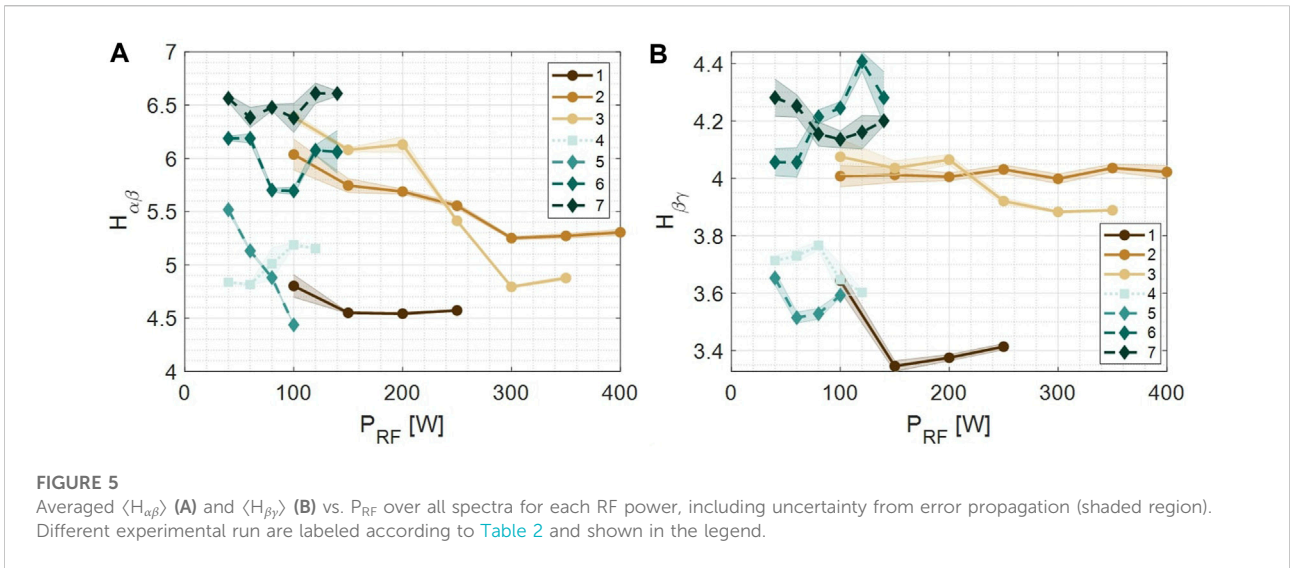
FIGURE 4 Monitoring of $H_{\alpha\beta}$ (A) and of $H_{\beta\gamma}$ (B) in the RF power (P_{RF} [W]) - spectra plane. Both refer to the experimental run 3, at $f_{RF} = 3.76$ GHz, $\rho_0 = 1E - 03$ mbar.

In Figures 5A,B the mean ratios given as from Eq. 7, and related uncertainties from the error analysis are shown as a function of RF power, for all the configurations examined. Considering the mean line-ratios and their experimental uncertainties, we therefore compared the latter to the theoretical ones, as resulting from numerical calculations using the Yacora CR model (Wunderlich et al., 2020). Theoretical ratios, $\mathcal{H}_{\alpha\beta}$ and $\mathcal{H}_{\beta\gamma}$, have been estimated for several electron densities ρ_e and energies (hereafter, temperature T_e , assuming a Maxwellian EEDF), and are shown in Figures 6A,B as surface plot in the $(\rho_e, k_B T_e)$ plane. On top of theoretical data, we drew the observed isoline ratios, collecting all the possible points (ρ_e, T_e) matching with the observable (solid line). The same is made for the upper and lower values of ratios - as coming from adding uncertainties from Eq. 8 - generating other possible points, and providing a range of solutions for the inverse problem of inferring ρ_e and T_e from the spectroscopic observables $H_{\alpha\beta, \beta\gamma}(\rho_e, T_e)$. In particular, a solution can be found by solving the following non-linear system

$$\begin{cases} \mathcal{H}_{\alpha\beta}(\rho_e, k_B T_e) = \langle H_{\alpha\beta} \rangle + \sigma_{\langle H_{\alpha\beta} \rangle} \\ \mathcal{H}_{\beta\gamma}(\rho_e, k_B T_e) = \langle H_{\beta\gamma} \rangle + \sigma_{\langle H_{\beta\gamma} \rangle} \end{cases} \quad (9)$$

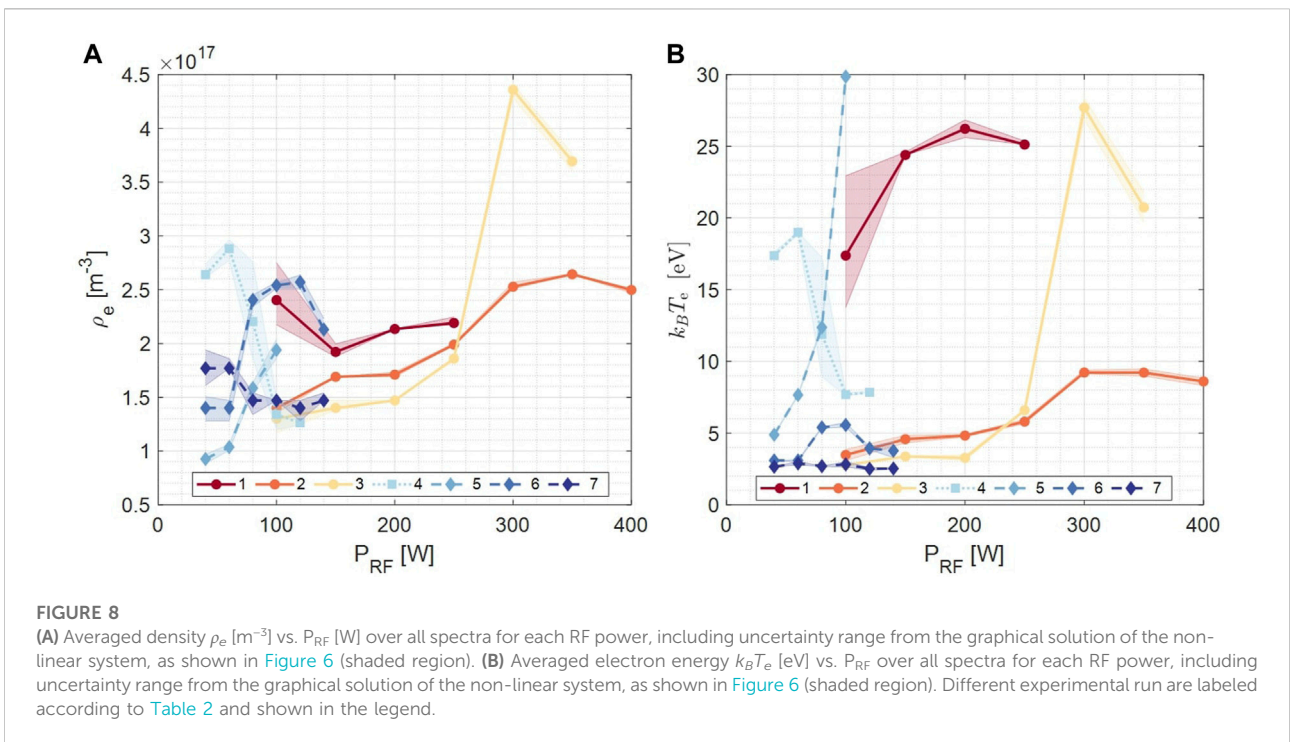
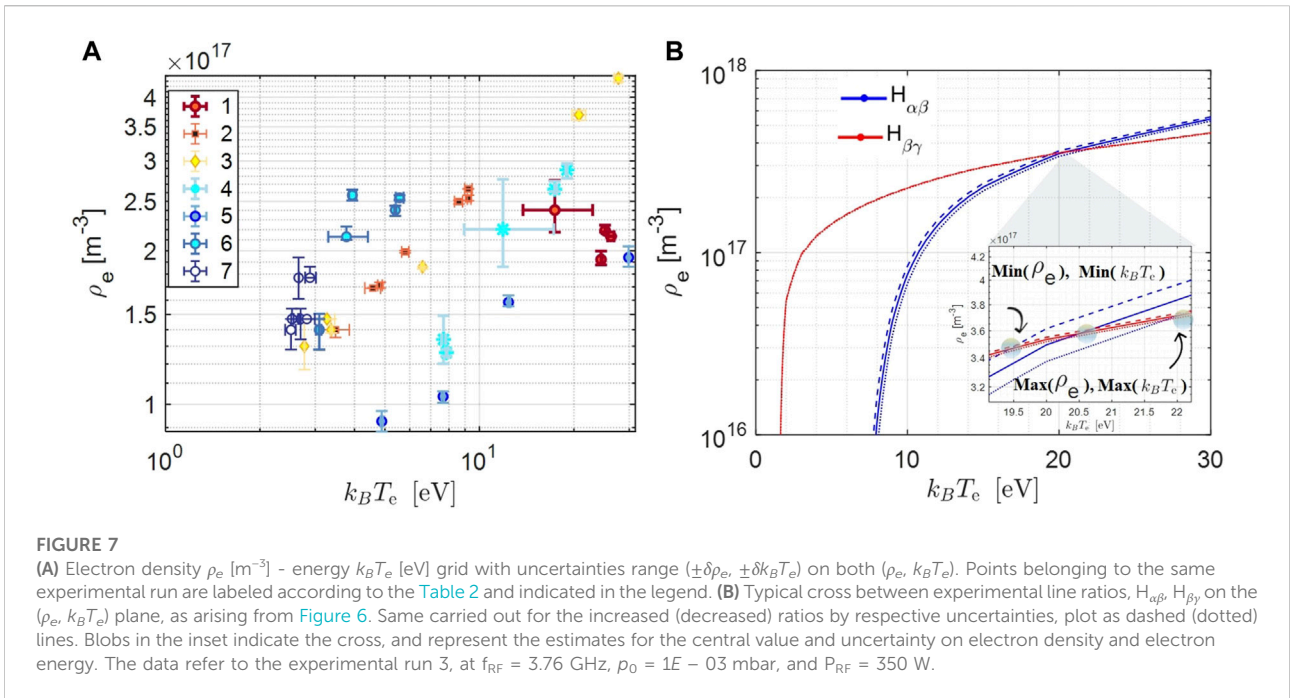
which if exists, should be unique. In other words, this is equivalent to find a cross-point in the (ρ_e, T_e) plane between the experimental isolines $H_{\alpha\beta}$ and $H_{\beta\gamma}$. If it exists, then a solution to the system of Eq. 9 exists too, and this provides an estimate of the averaged electron density and temperature, along the spectroscopic line-of-sight. The error committed in the estimates should be calculated propagating the uncertainties of measured ratios in the equation system. However, this is not an easy task to be accomplished. Beyond the degree of complexity in solving this uncertainty analysis, due to the non-linearity nature

of the problem, and to the lack of analytical functions describing both $\mathcal{H}_{\alpha\beta}$ and $\mathcal{H}_{\beta\gamma}$, determining the electron density and temperature uncertainties $\delta\rho_e, \delta k_B T_e$ is both analytically and numerically difficult. To make progress on it, we faced the problem from a different perspective. In particular, as it is shown in Figure 7B, we found upper and lower limits for both ρ_e and T_e from graphical solutions, as led by crosses of observed ratio uncertainties on the theoretical surface, that is, $H_{\alpha\beta} \pm \sigma_{\langle H_{\alpha\beta} \rangle}$, and $H_{\beta\gamma} \pm \sigma_{\langle H_{\beta\gamma} \rangle}$, as also shown in Figures 6A,B. These results deserve to be further discussed. First, the range of electron density and temperature found still represent line-convoluted average quantities, still suffering from the mentioned emission measure differential in temperature and density of structured plasmas (see Section 2.3.1), depicting global rather than local plasma parameters. Second, the line-ratio method carries several uncertainties due to relative intensities of the spectral features, which cannot be alternatively treated in this work, and which require absolute calibration of the instruments to improve the physical interpretation of OES data. The quality of the modeling results, on which relies the accuracy of diagnostic outcome by the line-ratio method, also depends on the existence and quality of cross section and rate coefficient data for the CR processes. As it can be evinced by Figure 7A, derived plasma parameters from OES measurements are generally affected by small uncertainties, especially in the low- T_e region ($k_B T_e \leq 10$ eV), in contrast to those belonging to the high- T_e range, for which error bars are larger (up to 50% relative error, see Table 4). This can be partially addressed to the theoretical trend of ratio isolines on the $(\rho_e, k_B T_e)$ plane, which for higher values of $k_B T_e$ bend into a quasi-flat curve. Thus, assuming even a small $\delta\rho_e$, a larger $\delta k_B T_e$ could be expected, and therefore a large range of possible crossed electron temperatures. Contrarily, in the low- T_e range, small uncertainties $\delta k_B T_e$ could



lead to a larger $\delta\rho_e$, and thus to a large range of possible crossed densities. Moreover, looking at Figures 8A,B other important features on plasma parameters dependencies on RF power and neutral gas pressure can be evinced. Generally, the low-pressure configurations (1, 4, and 5) show the largest temperatures, whereas high-pressure ones largely decrease the electron temperature. This effect could be explained in terms of a larger number of collisions in the plasma chamber upon increasing the pressure, which thermalize electrons, hence

providing a low-shifting of the EEDF peak. On the other side, upon increasing the RF power, there is an expected enhancement of T_e (see e.g., cfigs. 2,3) proportional to the electric field strength increasing with microwave power. Moreover, an increase of electron density, more likely driven by a combination of power- and pressure-dependent parameters such as *cyclotron electron number density*, neutral gas density supplied at the ECR zone, and gas flow rate within the ECR zone, is shown. These are very sensitive to the electromagnetic power released by

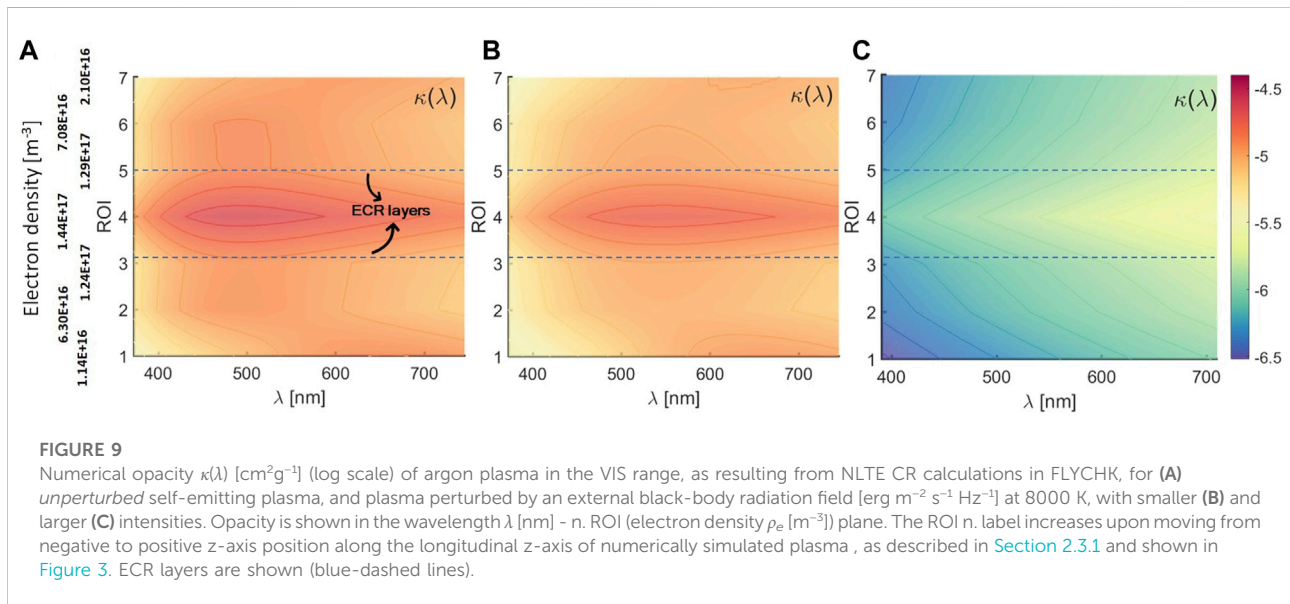


propagating microwaves in plasma and heating cyclotron electrons. Further observations can be provided by considering the RF frequency tuning and the different magnetic confinement adopted in each of the configurations.

By increasing the microwave frequency from ~ 3.76 GHz (cfigs. 1–3) to ~ 6.78 GHz (cfigs. 4–7), we shifted up the density cut-off by almost a factor 4, going from $1.76 \cdot 10^{17} \text{ m}^{-3}$ to $5.71 \cdot 10^{17} \text{ m}^{-3}$, respectively, which allowed to push up the electron density even

TABLE 3 Plasma parameters, *electron density* ρ_e [m^{-3}], and energy $k_B T_e$ [eV], estimated from numerical simulations along the longitudinal z-axis of the plasma chamber, for argon plasma confined in minimum-B-field, sustained by 12.84 GHz frequency and microwave power of 30 W.

	ROI 1	ROI 2	ROI 3	ROI 4	ROI 5	ROI 6	ROI 7
ρ_e [10^{17} m^{-3}]	0.114	0.630	1.24	1.44	1.30	0.707	0.210
$k_B T_e$ [eV]	38.10	100.10	140.40	112.50	138.30	103.40	46.80



if dealing with lower RF powers. Excluded few cases at large RF powers, where the electron density estimates slightly overcomes the cut-off (e.g., cfig. 3), the remaining cases do not overcome the cut-off values. In addition, a change in the axial magnetic field profile modifies the confinement, then influencing the electron heating efficiencies and plasma stability (Mazzaglia et al., 2018). Finally, in some of the configurations explored, we made use of a small amount of Ar gas (1%) as contaminant and tracer, adequately dosed by means of the RGA system described in Section 2.2.1, with the intent to make self-consistent cross-measurements of density from both H-lines and Ar-lines, assuming that theoretical hydrogen line-ratios are still comparable with the spectral outcome from this mixture. Beyond the Ar-lines analysis, which is missing in this article and still under analysis, one could preliminarily speculate on possible beneficial effects led by the Ar component in the H_2 -gas buffer. In particular, concerning the decrease of electron temperature observed in the cfig. 7 with respect the cfig. 6, possibly due to non-resonant interactions between the species (Phelps, 1992) (e.g., charge exchanges, gas mixing effects (Antaya, 1989; Delaunay, 1992; Tarvainen et al., 2005)). Indeed, collisions of H with Ar are peculiar because of the

very large cross sections for excitation of the H atoms at low energies (Phelps, 1992). Moreover, gas mixing beneficial impact has long been discussed in the ECR ion source community, explained through the energy exchange between the lighter and heavier species, with the heavier ones cooled down (ion cooling mechanism (Tarvainen et al., 2005)). This leads to a better confinement of the heavier species, while deteriorates that one of the lighter species. In our case, the mixing-driven deconfinement of H atoms might lead to a depletion of the reservoir of excited H atoms, which should turn into a decreasing intensity of emission line. This fact seems compatible with what observed, as it is shown in Figures 2B,C looking at the H_α line. However, further studies are necessary for sounder conclusions on the electron temperature decreasing mechanism, making use of absolutely calibrated spectra, which would certainly shed light on these properties. To conclude, among the several characterized plasmas, the most promising plasma parameters for the envisaged opacity measurements in the context of the blue-KN ejecta stage have been collected within the high-frequency and high-pressure cases (cfigs. 6 and 7), with electron temperature close to few eV and densities suitable to the astrophysical scenario.

TABLE 4 Plasma parameters (electron density ρ_e [m^{-3}], and energy $k_B T_e$ [eV]), estimated from OES measurements for different experimental configurations, in terms of B -field (Injection, Mid, and Extraction coil polarized current) [(a): 240 A, 0 A, 180 A; (b): 448 A, 45 A, 350 A; (c): 410 A, -80 A, 345 A], RF frequency (f_{RF} [GHz]), gas pressure p_0 [mbar], and RF power P_{RF} [W]. Gradient-color (red–white–blue) provides indications on the energy (temperature) gradient (■ hotter, ■ colder) for the many configurations explored. Gas-mixture cases are explicitly reported in the table.

	B	f_{RF}	p_0							
P_{RF}	(a)	3.76	$9E-04$	100	150	200	250			
ρ_e	H₂			$2.40_{+2.75}^{-2.17}E17$	$1.92_{-1.87}^{+2.00}E17$	$2.13_{-2.13}^{+2.13}E17$	$2.19_{-2.17}^{+2.24}E17$			
$k_B T_e$				$17.38_{+22.94}^{-13.76}$	$24.40_{+24.45}^{+24.60}$	$26.22_{+26.84}^{-25.61}$	$25.12_{+25.36}^{+25.26}$			
P_{RF}	(a)	3.76	$1E-02$	100	150	200	250	300	350	400
ρ_e	H₂			$1.40_{-1.40}^{-1.35}E17$	$1.69_{-1.69}^{+1.69}E17$	$1.71_{-1.69}^{+1.74}E17$	$1.99_{-1.98}^{+2.00}E17$	$2.53_{-2.51}^{+2.57}E17$	$2.64_{-2.64}^{+2.65}E17$	$2.50_{-2.47}^{+2.51}E17$
$k_B T_e$				$3.48_{+3.85}^{-3.08}$	$4.56_{+4.85}^{-4.31}$	$4.83_{+4.90}^{-4.75}$	$5.80_{+5.96}^{-5.65}$	$9.23_{+9.40}^{-9.15}$	$9.22_{+9.47}^{-8.98}$	$8.60_{+8.84}^{-8.32}$
P_{RF}	(a)	3.76	$1E-02$	100	150	200	250	300	350	
ρ_e	H₂⁽⁹⁹⁾			$1.30_{-1.17}^{+1.47}E17$	$1.40_{-1.38}^{+1.47}E17$	$1.47_{-1.47}^{+1.47}E17$	$1.86_{-1.84}^{+1.86}E17$	$4.36_{+4.41}^{-4.29}E17$	$3.69_{+3.77}^{-3.60}E17$	
$k_B T_e$	+Ar⁽¹⁾			$2.77_{+2.78}^{-2.76}$	$3.37_{+3.40}^{-3.35}$	$3.27_{+3.46}^{-3.09}$	$6.50_{+6.66}^{-6.49}$	$27.70_{+28.76}^{-26.88}$	$20.74_{+21.79}^{-19.72}$	
P_{RF}	(b)	6.774	$1E-03$	40	60	80	100	120		
ρ_e	H₂			$2.64_{-2.61}^{+2.74}E17$	$2.88_{-2.77}^{+2.96}E17$	$2.20_{+2.76}^{-1.86}E17$	$1.34_{-1.20}^{+1.49}E17$	$1.26_{-1.24}^{+1.28}E17$		
$k_B T_e$				$17.37_{+17.53}^{+17.63}$	$19.00_{-18.83}^{+19.02}$	$11.88_{+17.25}^{-8.94}$	$7.69_{-7.58}^{+7.81}$	$7.85_{+7.89}^{-7.83}$		
P_{RF}	(c)	6.786	$1E-03$	40	60	80	100			
ρ_e	H₂			$0.93_{-0.88}^{+0.97}E17$	$1.03_{-0.97}^{+1.06}E17$	$1.58_{-1.01}^{+1.63}E17$	$1.94_{-1.56}^{+2.04}E17$			
$k_B T_e$				$4.88_{+4.92}^{-4.84}$	$7.66_{+7.71}^{-7.58}$	$12.37_{+12.54}^{-12.33}$	$29.86_{-29.75}^{+29.99}$			
P_{RF}	(c)	6.786	$1E-02$	40	60	80	100	120	140	
ρ_e	H₂			$1.40_{+1.86}^{+1.50}E17$	$1.40_{-1.28}^{+1.47}E17$	$2.40_{-2.34}^{+2.45}E17$	$2.54_{-2.51}^{+2.57}E17$	$2.57_{-2.51}^{+2.63}E17$	$2.13_{+2.10}^{+2.23}E17$	
$k_B T_e$				$3.09_{-3.08}^{-3.09}$	$3.09_{+3.14}^{-3.01}$	$5.40_{+5.43}^{-5.35}$	$5.56_{+5.74}^{-5.41}$	$3.93_{+4.05}^{-3.84}$	$3.77_{+4.42}^{-3.30}$	
P_{RF}	(c)	6.786	$1E-02$	40	60	80	100	120	140	
ρ_e	H₂⁽⁹⁹⁾			$1.77_{-1.61}^{+1.94}E17$	$1.77_{-1.77}^{+1.86}E17$	$1.47_{-1.34}^{+1.54}E17$	$1.47_{-1.47}^{+1.47}E17$	$1.40_{-1.28}^{+1.47}E17$	$1.47_{-1.47}^{+1.54}E17$	
$k_B T_e$	+Ar⁽¹⁾			$2.65_{+2.66}^{-2.65}$	$2.88_{+3.01}^{-2.78}$	$2.69_{+2.70}^{-2.67}$	$2.82_{+2.99}^{-2.64}$	$2.51_{+2.60}^{-2.40}$	$2.53_{+2.56}^{-2.51}$	

3.2 Numerical results on optical properties

The numerical results on the plasma opacity performed by using FLYCHK for the argon plasma as structured from self-consistent simulations are presented and discussed here. Despite no numerical data are available yet on plasma conditions that could be suitable for opacity measurements, like those at high-pressure and low-power, which could provide under-dense and low-temperature plasmas in FPT, as shown in Section 3.1, the main goal for the moment is to demonstrate that we are able to unfold non-uniform plasma data collection. The latter in order to get reliable results from the observable that we need to measure: the opacity. Thus, according to the numerical tools we have described in Section 2.3.1, it is more straightforward to start from a higher energy content plasma than it is actually needed. In Table 3 we report on the density and temperature numerically estimated for each of the ROIs considered along the line-of-sight. As it can be evinced, there is a gradual increase of density upon moving toward the center of the chamber axis (ROI 4), where the plasmoid core is expected to be more dense, with respect to the external (halo) region. The same ROI presents a higher temperature compared to the external ROIs, however smaller if compared with neighboring ones, ROI 3 and 5, which correspond to the ECR layer and to the regions maximizing the electron heating, thus their energy. Because of the relative high electron temperature, the total amount of opacity in the VIS range turns out to be very low ($\kappa < 10^{-4} \text{ cm}^2\text{g}^{-1}$), as it is possible to observe in Figure 9. Indeed, electrons with hundreds of eV of energy will impact more on level population distribution and atomic line transitions belonging to higher energy states, in the soft-X-ray emission range, which is out of the EM range of interest for this work. The influence of higher-density ROIs in Figure 9 is also highlighted, where as expected the most opaque plasma arises from the inner plasmoid region in between of the ECR layers. Furthermore, we also explored the influence of an external black-body radiation field to the plasma opacity, which results are shown in Figures 9B,C, with a photon flux of $\sim 10^{25} \text{ s}^{-1}\text{m}^{-2}$, and $\sim 10^{32} \text{ s}^{-1}\text{m}^{-2}$, respectively. An important effect can be evinced with respect to the unperturbed plasma opacity shown in Figure 9A (i.e., without any external radiation field), especially in the case of the largest photon flux affecting the plasma source - see Figure 9C. Here, the opacity decreases by 1–2 orders of magnitudes ($\kappa < 10^{-5} \text{ cm}^2\text{g}^{-1}$). This phenomenon can be explained by a radiation-driven progressive de-population mechanism of lower energy levels for given atomic transition lines, thus reducing N_ℓ and tending to equilibrate the latter to the corresponding upper level density population, $N_{u\ell}$, which accordingly to Eq. 3 pushes the system in the limit of zero opacity (i.e., transparent plasma) upon increasing the radiation field intensity. An analysis of the occupation number of energy levels, as resulting from FLYCHK calculations, has confirmed this hypothesis. We have extended calculations of synthetic opacity to further study the impact of external black-body

radiations on the latter, for gaseous as well as for metallic species of interest for the KN studies. In doing this, we have considered measured electron density and temperature from OES, in particular studying, the case of plasma from cfg. 7 at $P_{RF} = 120 \text{ W}$, neglecting for a moment the plasma stratification problem. Input plasma parameters are considered from estimates in Table 4. We started by studying the gaseous case (Ar), which results for the opacity contribution are shown in Figure 10. As it is possible to observe in Figure 10A, numerical opacity at this temperature is extremely larger ($\kappa \lesssim 1 \text{ cm}^2\text{g}^{-1}$) if compared with results shown in Figure 9, effect apparently only due to the lower temperature. Indeed, at higher plasma temperature, the opacity largely decreases as expected from the energy shifting of absorption transition lines led by more energetic electrons, as shown in Figure 10B, also changing the expected dependency on the wavelength. An increasing radiation field intensity similar to that shown in Figure 9 impacts on the opacity terms, which quickly drops down of several orders of magnitude. Looking at metallic species, we performed the same calculations for the argon plasma, but considering metallic plasmas made of selenium, strontium, zirconium, and niobium, among the most favored elements for the experimental measurements. Results are shown in Figure 11, where both low-temperature (top row) and high-temperature (bottom row) cases are shown. All the self-emitting metallic plasmas (no external photon flux) are extremely opaque, with $\kappa \sim 10^3 \text{ cm}^2\text{g}^{-1}$. Including a radiation field, slightly impacts these numbers, unless one goes for sources with a high photon flux ($\sim 10^{32} \text{ s}^{-1}\text{m}^{-2}$), which would decrease such values. As similar to results obtained for the argon plasma, by increasing the electron temperature, the opacity decreases several orders of magnitude. This is not the case of niobium opacity, which seems to be enhanced in the case of hotter plasma, likely due to an increasing complexity of electronic shells. To conclude, the numerical investigation has highlighted peculiar modification of plasma opacity led by a structured ECR plasma, providing numerical predictions of the latter, accordingly to the atomic database on argon transitions, which could support future experimental measurements in gaseous plasmas. Further investigations, extending the method by giving additional inputs to FLYCHK for more precise calculations, for example, the ECR charge state distribution expected for metallic/gaseous plasmas, which numerical study is under development (Mishra et al., 2020), will produce outputs more tight to real scenarios achievable with experiments. Thus, having access to layered optical properties of the plasma would help in deconvolving the stratified emission, otherwise only partially decoded by the inverse problem techniques, and still suffering from residual large uncertainties. Finally, numerical simulations of opacity under experimentally explored plasma conditions, and close to the blue-KN ejecta parameters, can certainly support the dimensioning of light source features for future transmission spectroscopic measurements, finding a good trade-off between the source and its transparency through the plasma.

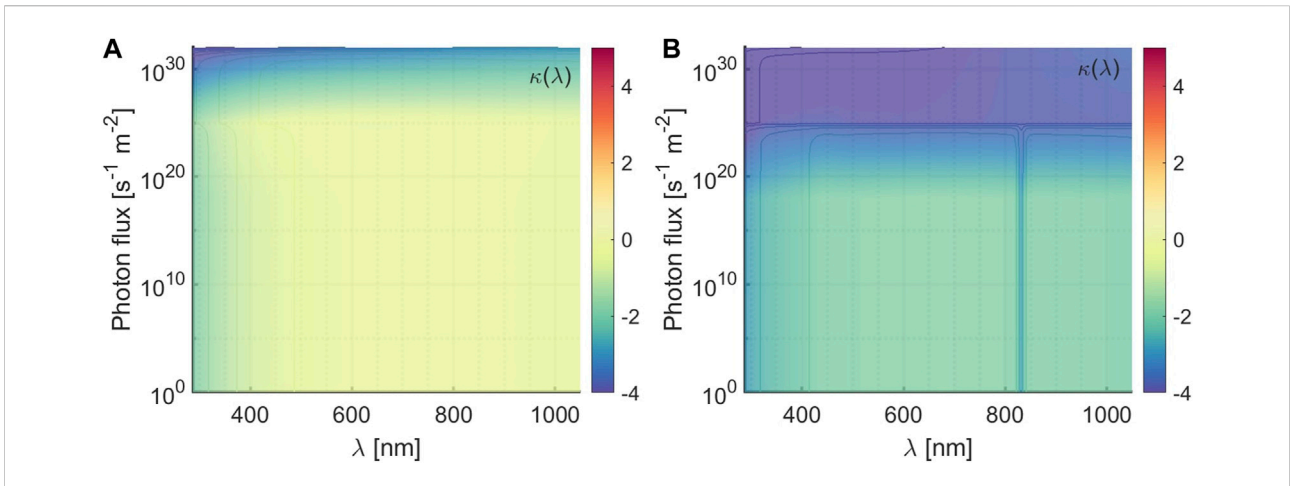


FIGURE 10 Numerical opacity $\kappa(\lambda)$ [cm^2g^{-1}] (log scale) of argon plasma in the VIS range, as resulting from NLTE CR calculations in FLYCHK, at electron density $\rho_e = 1.4 \cdot 10^{17} \text{ m}^{-3}$, and energy of (A) $k_B T_e = 2.43 \text{ eV}$, and (B) $k_B T_e = 7.88 \text{ eV}$. Opacity is shown in the wavelength λ [nm] - external radiation photon flux $\text{s}^{-1}\text{m}^{-2}$ plane. Plasma parameters of (A) have been selected from OES data from cfg. 7, at $P_{RF} = 120 \text{ W}$ (see Table 4), while for (B) the density has been maintained equal and the energy increased.

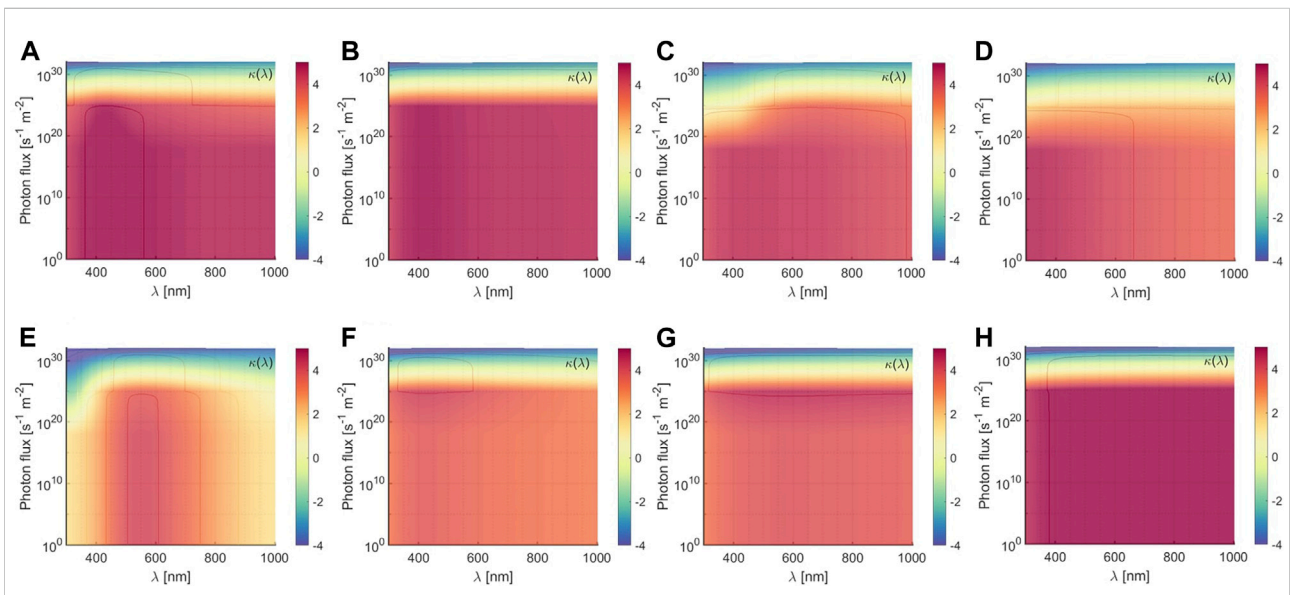


FIGURE 11 Numerical opacity $\kappa(\lambda)$ [cm^2g^{-1}] (log scale) of metallic plasmas in the VIS range, as resulting from NLTE CR calculations in FLYCHK, for (A,E) selenium (Se), (B,F) strontium (Sr), (C,G) zirconium (Zr), and (D,H) niobium (Nb), at electron density $\rho_e = 1.4 \cdot 10^{17} \text{ m}^{-3}$, and energy $k_B T_e = 2.43 \text{ eV}$ (A–D), and $k_B T_e = 7.88 \text{ eV}$ (E–H). Opacity is shown in the wavelength λ [nm] - external radiation photon flux $\text{s}^{-1}\text{m}^{-2}$ plane.

4 Conclusion

In this work, we have reported on the first experimental attempt of reproducing kilonovae ejecta plasma conditions, carried out on the Flexible Plasma Trap at the INFN-LNS. The kilonovae signal plays a fundamental role in the multi-messenger astronomy, entering in a sophisticated GW-detecting

network and delivers precious information on the composition and dynamics of the neutron-rich post-merger plasma ejecta. The ejecta opacity largely impacts on the kilonovae study, with consequent highly demanded experimental efforts to make progresses on the kilonovae opacity characterization. The novel work so far performed on *under-dense* and *low-temperature* magneto-plasmas opens the route for the first-of-

its-kind in-laboratory plasma opacity measurements of metallic plasma species relevant for kilonovae light curve studies, foreseen within the PANDORA project. Plasma parameter measurements have provided sounder bases for the reproducibility under early-stage kilonovae conditions and also benchmarked the efficiency of plasma diagnostics. Numerical efforts have been also spent to support future opacity measurements, by looking at the radiation–plasma matter interactions in the framework of highly inhomogeneous and anisotropic magnetically confined ECR plasmas. A synergistic use of spectroscopic measurements and numerical tools allowed to give some hints on typical light source to be employed in transmission spectroscopic measurements, designed for the future opacity measurements of light r -process element plasmas interesting for the kilonovae study. Experimental electron density and temperature obtained for high-pressure and high-frequency ECR plasmas are the most promising among the totality of experimental configurations explored, encouraging to extend experimental characterizations at larger pressures, in order to further decrease the average electron temperature, and hence to better reproduce conditions of the blue-kilonovae stage. The use of argon as contaminant looks promising for two reasons: first, an apparent beneficial effect as a thermal regulator in these plasmas, which requires further investigations; second, having theoretical line-ratios for argon line transitions will allow to make cross-check on the plasma parameters estimates arising from the hydrogen spectra analysis, thus providing more robust results. On the other side, numerical results have highlighted the influence on plasma opacity led by layered plasma parameters in the space, with important consequences for the convoluted line emission detected along the spectroscopic line-of-sight. Moreover, the study of the influence of external radiation acting on the plasma source optical observables has shown peculiar effects in terms of tuning the plasma opacity, accordingly to the level population of atoms involved, dependent on the electronic shell configurations and plasma temperature. Further numerical investigations are planned, extending CR calculations performed to three-dimensional properties of ECR plasmas, including spatial-dependent charge state distribution and ions residence time due to the magnetic confinement, not taken into account in the FLYCHK code suite. Next experimental steps are planned to perform opacity measurements of gaseous and metallic plasma sources based on the plasma trap configurations reported in this work.

References

- Abbott, B. P., Abbott, R., Abbott, T. D., Acernese, F., Ackley, K., Adams, C., et al. (2017). GW170817: Observation of gravitational waves from a binary neutron star inspiral. *Phys. Rev. Lett.* 119, 161101. doi:10.1103/PhysRevLett.119.161101
- Antaya, T. A. (1989). A review of studies for the variable frequency superconducting ecr ion source project at msu. *J. Phys. Colloq.* 50, C1-707–C1-726. doi:10.1051/jphyscol:1989176

Data availability statement

The original contributions presented in the study are included in the article/Supplementary Material; further inquiries can be directed to the corresponding author.

Author contributions

Conceptualization: AP, DM SC, ML, AP, and DV. Numerical simulations: AP, MB, GE, BM, and AG. Experimental data: AP, GE, MB, MM, BM, SM, DM GM, GF, EN, DS, and GT. Data analysis: AP, MB, GE, MM, DM, and BM. Funding acquisition: DM and DS. Writing—original draft: AP. Writing—review and editing: AP, DM, SC, DV, AG, AT, RS, GE, MB, BM, ML, and AP. All authors have read and agreed to the published version of the manuscript.

Acknowledgments

The authors wish to thank INFN for the support through the project PANDORA Gr3 funded by third Nat. Sci. Comm. and the whole PANDORA collaboration. DV acknowledges the financial support from the German-Israeli Foundation (GIF No. I-1500–303.7/2019).

Conflict of interest

The authors declare that the research was conducted in the absence of any commercial or financial relationships that could be construed as a potential conflict of interest.

Publisher's note

All claims expressed in this article are solely those of the authors and do not necessarily represent those of their affiliated organizations, or those of the publisher, the editors, and the reviewers. Any product that may be evaluated in this article, or claim that may be made by its manufacturer, is not guaranteed or endorsed by the publisher.

- Arcavi, I., Hosseinzadeh, G., Howell, D. A., McCully, C., Poznanski, D., Kasen, D., et al. (2017). Optical emission from a kilonova following a gravitational-wave-detected neutron-star merger. *Nature* 551, 64–66. doi:10.1038/nature24291

- Bailey, J. E., Nagayama, T., Loisel, G. P., Rochau, G. A., Blancard, C., Colgan, J., et al. (2015). A higher-than-predicted measurement of iron opacity at solar interior temperatures. *Nature* 517, 56–59. doi:10.1038/nature14048

- Bailey, J. E., Rochau, G. A., Mancini, R. C., Iglesias, C. A., MacFarlane, J. J., Golovkin, I. E., et al. (2009). Experimental investigation of opacity models for stellar interior, inertial fusion, and high energy density plasmas. *Phys. Plasmas* 16, 058101. doi:10.1063/1.3089604
- Barnes, J., and Kasen, D. (2013). Effect of a high opacity on the light curves of radioactively powered transients from compact object mergers. *Astrophys. J.* 775, 18. doi:10.1088/0004-637x/775/1/18
- Barnes, J., Kasen, D., Wu, M. R., and Martínez-Pinedo, G. (2016). Radioactivity and thermalization in the ejecta of compact object mergers and their impact on kilonova light curves. *Astrophys. J.* 829, 110. doi:10.3847/0004-637x/829/2/110
- Chung, H. K., Chen, M., Morgan, W., Ralchenko, Y., and Lee, R. (2005). Flychk: Generalized population kinetics and spectral model for rapid spectroscopic analysis for all elements. *High. Energy Density Phys.* 1, 3–12. doi:10.1016/j.hedp.2005.07.001
- Craig, I. J. D., and Brown, J. C. (1976). Fundamental limitations of X-ray spectra as diagnostics of plasma temperature structure. *Astronomy Astrophysics* 49, 239–250.
- Delaunay, M. (1992). Influence of ionization cross sections on the gas mixing effect for the production of ar⁹⁺ ions in a caprice ecr source. *Rev. Sci. Instrum.* 63, 2861–2863. doi:10.1063/1.1142778
- Domoto, N., Tanaka, M., Wanajo, S., and Kawaguchi, K. (2021). Signatures of r-process elements in kilonova spectra. *Astrophys. J.* 913, 26. doi:10.3847/1538-4357/abf358
- Fantz, U. (2006). Basics of plasma spectroscopy. *Plasma Sources Sci. Technol.* 15, S137–S147. doi:10.1088/0963-0252/15/4/s01
- Fantz, U., Falter, H., Franzen, P., Wunderlich, D., Berger, M., Lorenz, A., et al. (2006). Spectroscopy—A powerful diagnostic tool in source development. *Nucl. Fusion* 46, S297–S306. doi:10.1088/0029-5515/46/6/s10
- Gammino, S., Celona, L., Mascali, D., Castro, G., Torrisi, G., Neri, L., et al. (2017). The flexible plasma trap (FPT) for the production of overdense plasmas. *J. Instrum.* 12, P07027. doi:10.1088/1748-0221/12/07/p07027
- Geller, R. (1996). *Electron cyclotron resonance ion sources and ECR plasmas*. United Kingdom: Institute of Physics.
- Gillanders, J. H., McCann, M., Sim, S., Smartt, S., and Ballance, C. P. (2021). Constraints on the presence of platinum and gold in the spectra of the kilonova at2017gfo. *Mon. Notices R. Astronomical Soc.* 506, 3560–3577. doi:10.1093/mnras/stab1861
- Gillanders, J. H., Smartt, S. J., Sim, S. A., Bauswein, A., and Goriely, S. (2022). Modelling the spectra of the kilonova at2017gfo – i: The photospheric epochs. doi:10.48550/ARXIV.2202.01786
- Hoarty, D. J., James, S. F., Brown, C. R. D., Williams, B. M., Guymer, T., Hill, M., et al. (2010). High temperature, high density opacity measurements using short pulse lasers. *J. Phys. Conf. Ser.* 244, 012002. doi:10.1088/1742-6596/244/1/012002
- Judge, P. G., Hubeny, V., and Brown, C. J. (1997). Fundamental limitations of emission-line spectra as diagnostics of plasma temperature and density structure. *Astrophys. J.* 475, 275–290. doi:10.1086/303511
- Judge, P. G., and Hubeny, V. (1995). Solution to the bivariate integral inversion problem: The determination of emission measures differential in temperature and density. *Astrophysical J.* 448, 61–64. doi:10.1086/309594
- Kasen, D., Metzger, B., Barnes, J., Quataert, E., and Ramirez-Ruiz, E. (2017). Origin of the heavy elements in binary neutron-star mergers from a gravitational-wave event. *Nature* 551, 80–84. doi:10.1038/nature24453
- Knoll, G. F. (2010). *Radiation detection and measurement*. 4th ed. New York, NY: Wiley.
- Korobkin, O., Rosswog, S., Arcones, A., and Winteler, C. (2012). On the astrophysical robustness of the neutron star merger r-process. *Mon. Notices R. Astronomical Soc.* 426, 1940–1949. doi:10.1111/j.1365-2966.2012.21859.x
- Li, L. X., and Paczyński, B. (1998). Transient events from neutron star mergers. *Astrophys. J.* 507, L59–L62. doi:10.1086/311680
- Mascali, D., Naselli, E., and Torrisi, G. (2022). Microwave techniques for electron cyclotron resonance plasma diagnostics. *Rev. Sci. Instrum.* 93, 033302. doi:10.1063/50075496
- Mascali, D., Santonocito, D., Amaducci, S., Andò, L., Antonuccio, V., Biri, S., et al. (2022). A novel approach to β -decay: Pandora, a new experimental setup for future in-plasma measurements. *Universe* 8, 80. doi:10.3390/universe8020080
- Mauro, G. S., Celona, L., Torrisi, G., Pidatella, A., Naselli, E., Russo, F., et al. (2022). An innovative superconducting magnetic trap for probing β -decay in plasmas. *Front. Phys.* 10. doi:10.3389/fphy.2022.931953
- Mazzaglia, M., Castro, G., Mascali, D., Briefi, S., Fantz, U., Celona, L., et al. (2018). Study of the influence of magnetic field profile on plasma parameters in a simple mirror trap. *J. Instrum.* 13, C11014. doi:10.1088/1748-0221/13/11/c11014
- Mazzaglia, M., Castro, G., Mascali, D., Celona, L., Neri, L., Torrisi, G., et al. (2019). Improvement of the characterization of the proton source for the European spallation source by means of optical emission spectroscopy. *Phys. Rev. Accel. Beams* 22, 053401. doi:10.1103/PhysRevAccelBeams.22.053401
- Metzger, B. D. (2019). *Kilonovae*. *Living Rev. Relativ.* 23, 1. doi:10.1007/s41114-019-0024-0
- Metzger, B. D., Martínez-Pinedo, G., Darbha, S., Quataert, E., Arcones, A., Kasen, D., et al. (2010). Electromagnetic counterparts of compact object mergers powered by the radioactive decay of r-process nuclei. *Mon. Not. R. Astron. Soc.* 406, 2650–2662. doi:10.1111/j.1365-2966.2010.16864.x
- Mishra, B., Galata, A., Pidatella, A., Racz, R., Biri, S., Torrisi, G., et al. (2020). “Modelling space-resolved ion dynamics in ECR plasmas for predicting in-plasma β -decay rates,” in *Frontiers in physics - research topics: Nuclear physics and astrophysics in plasma traps*. forthcoming (Lausanne, Switzerland: frontiers).
- Mishra, B., Pidatella, A., Biri, S., Galatà, A., Naselli, E., Racz, R., et al. (2021). A novel numerical tool to study electron energy distribution functions of spatially anisotropic and non-homogeneous ecr plasmas. *Phys. Plasmas* 28, 102509. doi:10.1063/5.0061368
- Naselli, E., Mascali, D., Biri, S., Caliri, C., Castro, G., Celona, L., et al. (2019). Multidiagnostics setups for magnetoplasmas devoted to astrophysics and nuclear astrophysics research in compact traps. *J. Instrum.* 14, C10008. doi:10.1088/1748-0221/14/10/c10008
- Naselli, E., Mascali, D., Mazzaglia, M., Biri, S., Racz, R., Pálinskás, J., et al. (2019). Impact of two-close-frequency heating on ECR ion source plasma radio emission and stability. *Plasma Sources Sci. Technol.* 28, 085021. doi:10.1088/1361-6595/ab32f9
- Naselli, E., Racz, R., Biri, S., Mazzaglia, M., Celona, L., Gammino, S., et al. (2022). Innovative analytical method for x-ray imaging and space-resolved spectroscopy of ecr plasmas. *Condens. Matter* 7, 5. doi:10.3390/condmat7010005
- Naselli, E., Racz, R., Biri, S., Mazzaglia, M., Galatà, A., Celona, L., et al. (2022). Quantitative analysis of an ECR ar plasma structure by x-ray spectroscopy at high spatial resolution. *J. Instrum.* 17, C01009. doi:10.1088/1748-0221/17/01/c01009
- Perego, A., Rosswog, S., Cabezón, R. M., Korobkin, O., Käppeli, R., Arcones, A., et al. (2014). Neutrino-driven winds from neutron star merger remnants. *Mon. Notices R. Astronomical Soc.* 443, 3134–3156. doi:10.1093/mnras/stu1352
- Perego, A., Vescovi, D., Fiore, A., Chiesa, L., Vogl, C., Benetti, S., et al. (2022). Production of very light elements and strontium in the early ejecta of neutron star mergers. *Astrophys. J.* 925, 22. doi:10.3847/1538-4357/ac3751
- Phelps, A. V. (1992). Collisions of h⁺, h₂⁺, h₃⁺, arh⁺, h-h, and h₂ with ar and of ar⁺ and arh⁺ with h₂ for energies from 0.1 ev to 10 kev. *J. Phys. Chem. Reference Data* 21, 883–897. doi:10.1063/1.555917
- Pidatella, A., Cristallo, S., Galatà, A., La Cognata, M., Mazzaglia, M., Perego, A., et al. (2021). In-plasma study of opacity relevant for compact binary ejecta. *Il Nuovo Cimento C* 44, 4. doi:10.1393/NCC/I2021-21065-X
- Racz, R., Biri, S., Pálinskás, J., Mascali, D., Castro, G., Caliri, C., et al. (2016). X-ray pinhole camera setups used in the atomki ecr laboratory for plasma diagnostics. *Rev. Sci. Instrum.* 87, 02A741. doi:10.1063/1.4933085
- Rosswog, S. (2015). The multi-messenger picture of compact binary mergers. *Int. J. Mod. Phys. D* 24, 1530012. doi:10.1142/S0218271815300128
- Tanaka, M., Kato, D., Gaigalas, G., and Kawaguchi, K. (2020). Systematic opacity calculations for kilonovae. *Mon. Not. R. Astron. Soc.* 496, 1369–1392. doi:10.1093/mnras/staa1576
- Tarvainen, O., Suominen, P., Ropponen, T., Kalvas, T., Heikkinen, P., and Koivisto, H. (2005). Effect of the gas mixing technique on the plasma potential and emittance of the jyfl 14 ghz electron cyclotron resonance ion source. *Rev. Sci. Instrum.* 76, 093304. doi:10.1063/1.2038647
- Taylor, J. R. (1996). *An introduction to error analysis: The study of uncertainties in physical measurements*. 2 sub edn. Sausalito, CA: University Science Books.
- Thompson, A. M., Brown, J. C., Craig, I. J. D., and Fulber, C. (1992). Inference of non-thermal electron energy distributions from hard X-ray spectra. *Astronomy Astrophysics* 265, 278–288.
- Torrisi, G., Naselli, E., Donato, L. D., Mauro, G., Mazzaglia, M., Mishra, B., et al. (2022). RF and microwave diagnostics for compact plasma traps and possible perspectives for fusion devices. *J. Instrum.* 17, C01050. doi:10.1088/1748-0221/17/01/c01050
- Watson, D., Hansen, C. J., Selsing, J., Koch, A., Malesani, D. B., Andersen, A. C., et al. (2019). Identification of strontium in the merger of two neutron stars. *Nature* 574, 497–500. doi:10.1038/s41586-019-1676-3
- Wu, Z., Ricigliano, G., Kashyap, R., Perego, A., and Radice, D. (2022). Radiation hydrodynamics modelling of kilonovae with SNEC. *Mon. Not. R. Astron. Soc.* 512, 328–347. doi:10.1093/mnras/stac399
- Wunderlich, D., Giacomini, M., Ritz, R., and Fantz, U. (2020). Yacora on the web: Online collisional radiative models for plasmas containing h, h₂ or he. *J. Quantitative Spectrosc. Radiat. Transf.* 240, 106695. doi:10.1016/j.jqsrt.2019.106695
- Zhang, J., Xu, Y., Yang, J., Yang, G., Li, H., Yuan, Z., et al. (2011). Opacity measurement of a gold plasma at T_e = 85 eV. *Phys. Plasmas* 18, 113301. doi:10.1063/1.3660407